Mode II fracture behavior of glass fiber composite-steel bonded interface–experiments and CZM

He, Pei; Koetsier, Mathieu; Mylonopoulos, Vasileios; Pavlovic, Marko

DOI
10.1016/j.engfracmech.2024.110510

Publication date
2024

Document Version
Final published version

Published in
Engineering Fracture Mechanics

Engineering Fracture Mechanics 310 (2024) 110510

Contents lists available at ScienceDirect

Engineering Fracture Mechanics

journal homepage: www.elsevier.com/locate/engfracmech

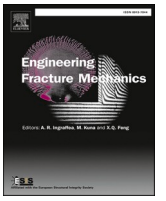

Mode II fracture behavior of glass fiber composite-steel bonded interface–experiments and CZM

Pei He, Mathieu Koetsier, Vasileios Mylonopoulos, Marko Pavlovic *

Faculty of Civil Engineering and Geosciences, Delft University of Technology, Netherlands

ARTICLE INFO

Keywords:
Composite-steel bonded interface
3ENF and 4ENF
DIC
Four-linear traction-separation law
CZM

ABSTRACT

The dominant failure mode was characterized as debonding in the novel non-welded wrapped composite joint made with GFRP composites wrapped around steel sections. Glass fiber composite-steel three-point end notched flexure (3ENF) and four-point end notched flexure (4ENF) specimens were utilized to experimentally investigate mode II fracture behavior of this composite-steel bonded interface. Two new methods were proposed with the help of digital image correlation (DIC) technique to quantify fracture data during the tests: 1) the "shear strain scaling method" to quantify the crack length *a*; 2) the asymptotic analysis method based on the longitudinal displacement distribution along the height of the specimen at the pre-crack tip to quantify the crack tip opening displacement (CTOD). To numerically simulate the mode II fracture behavior, a four-linear traction-separation law was proposed in the cohesive zone modeling (CZM) where the softening behavior with a plateau was defined by the authors between traditionally considered initiation and fiber bridging behavior. The experimental and numerical approaches were validated mutually through good matches between the test and FEA results. 3ENF test provided good insight into softening behavior while 4ENF contributed to quantification of fiber bridging. These findings contribute to a more comprehensive characterization and understanding of the ductile fracture behavior of bi-material bonded joints, especially in mode II failure scenarios.

1. Introduction

The concept of non-welded wrapped composite joints was proposed by TU Delft [1] as an alternative to traditional welded joints, as shown in Fig. 1a). It aims to fully unlock the application potential of circular hollow sections (CHS) restricted by the low fatigue endurance of current welding joining technology in many structural applications. Using this novel joining technology, CHS brace members (diagonals) and the chord member are bonded together by the composite wrap which can be shaped in an optimal manner to decrease stress concentration at the bonded interface. The tensile static tests of wrapped composite joints showed improved initial stiffness and equivalent load resistance compared to welded joints [2] while the subsequent fatigue experiments validated their lower stiffness degradation and superior fatigue life than welded counterparts [3]. Debonding of the composite-steel bonded interface was found to be the predominant failure mode of wrapped composite joints subjected to axial load [2], as shown in Fig. 1b). It is therefore imperative to understand the fracture behavior of the composite-steel bonded interface as a prerequisite for prediction of the joint resistance. An interfacial crack can propagate in three different fracture modes in fracture mechanics: mode I (opening), mode II (in-

* Corresponding author.
E-mail address: M.Pavlovic@tudelft.nl (M. Pavlovic).

https://doi.org/10.1016/j.engfracmech.2024.110510
Received 5 June 2024; Received in revised form 14 August 2024; Accepted 17 September 2024
Available online 21 September 2024

Nomenclature

CHS	circular hollow section
3ENF	the three-point end notched flexure test
4ENF	the four-point end notched flexure test
DIC	digital image correlation
CTOD	crack tip opening displacement
CZM	cohesive zone modeling
h_{steel}, $h_{composite}$	thickness of the steel adherend and the composite adherend, respectively
l, B and L	the specimen length, specimen width and the half span length, respectively
d	the distance of the two loading pins in 4ENF specimens
a_0, a	the pre-crack length, the present crack length, respectively
Sq	the root mean square roughness
"p"	onset of plasticity
"c"	onset of cracking
"b"	onset of fiber bridging
"f"	failure
SERR	strain energy release rate
FPZ	fracture process zone
δ_p, δ_c, δ_b, δ_f	CTOD at the stage of "p", "c", "b", "f"
σ_p, σ_c, σ_b, σ_f	cohesive traction at the stage of "p", "c", "b", "f"
$G_{IIc,tip}$, $FPZ_{IIc,tip}$	The critical SERR and the FPZ length at crack initiation
$G_{IIc,soft}$, $FPZ_{IIc,soft}$	The SERR and the FPZ length due to softening
$G_{IIc,br}$, $FPZ_{IIc,br}$	The SERR and the FPZ length due to fiber bridging
G_{IIc}, FPZ_{IIc}	The critical SERR and the FPZ length for crack propagation
EGM	the extended global method
E_{steel}, I_{steel}, $E_{composite}$, $I_{composite}$	elastic modulus and moment of inertia of steel and composite adherends
EI	the equivalent elastic modulus and moment of inertia of the specimen
β	the equivalent longitudinal strain ratio
Ψ	the bending stiffness ratio of steel and composite adherends
A_{steel}, $A_{composite}$	the cross-section area of the steel and composite adherends
z_{steel}, $z_{composite}$	the centroid z coordinates of the steel and composite adherends
z	the coordinate of the equivalent centroid of the specimen cross-section
F	the applied load
M_{steel}, $M_{composite}$	the bending moment applied to the steel and composite adherends
VCCT	the Virtual Crack Closure Technique
COF	coefficient of friction
CCM	The conventional compliance calibration method

plane shear) and mode III (out-of-plane shear), as illustrated in Fig. 2. Mode I failure was found pronounced at the secondary bonded interface (on the chord) and at the end of the primary bonded interface (on the brace). In contrast, mode II failure was observed governing at the root of the primary bonded interface (on the brace), leading to the coalescence of the debonding crack along the braces, as shown in Fig. 1b). In a parallel study, the mode I fracture behavior was investigated experimentally and numerically by using glass fiber composite-steel double cantilever beam (DCB) specimens [4]. In comparison, the current study focused on the mode II fracture behavior.

The three-point end notched flexure (3ENF) specimen configuration was initially proposed by Russel [5,6] and was widely established in the testing standards, such as ASTM D7905 [7], for evaluation of delamination in unidirectional composites under mode II loading. Many researchers have employed this configuration to acquire mode II fracture properties of the adhesively bonded joints or to assess the delamination toughness of composite laminate [8–11]. Nevertheless, an important feature of 3ENF configuration is that the crack propagation is generally unstable. Some researchers have found that stable crack growth can be achieved when the initial crack length is at least 0.7 times of the half span [12,13]. However, this finding is specific to the delamination crack initiation and propagation at the interply interfaces of the composite laminates or adhesively bonded joints. It is still unknown how to achieve stable crack growth in directly bonded composite-steel interfaces. Additionally, several authors have also reported that 3ENF test allows only for determining fracture behavior related to crack initiation but not the R-curve behavior [14,15], which characterizes the crack propagation. As an alternative, the four-point end notched flexure (4ENF) configuration was proposed to obtain stable crack growth in mode II loading scenario [16,17]. However, effect of friction was found to be significantly larger in 4ENF tests compare to 3ENF tests [18], posing a significant challenge in standardizing the 4ENF configuration.

It should be noted that all the experimental and numerical work mentioned above was conducted based on symmetric (same material and same thickness) 3ENF and 4ENF configurations. In the case of asymmetric configurations, with un-even thickness of

adherends around the interface and/or dissimilar materials, limited research studies have been conducted to investigate fracture behavior of 3ENF specimens [19–24]. No research studies regarding asymmetric 4ENF specimens have been reported – to the best of the authors' knowledge. The mode II fracture behavior of an asymmetric composite-metal bonded interface is complex due to three primary reasons: a) inherent mode mixity as a result of loading asymmetry and material asymmetry across the interface [25]; b) dependency of interfacial fracture behavior on the material and surface treatment of the adherends, types of resin and adhesive; c) non-linear behavior of the interface attributed to plastic deformation of the metal adherend where linear elastic fracture mechanics (LEFM) may not apply. To alleviate the mode mixity in ENF tests, basically two design criteria have been proposed in the literature:

1) pure mode II is achieved if the two adherends have equal axial strains along the interface [23,26–28];
2) pure mode II is achieved if the two adherends have equal bending rigidities [29–33].

More recently, F. Mujika et al. [34] performed mechanical modeling of asymmetric ENF specimens, validated by finite element analysis (FEA), and demonstrated the correctness of the design criteria 1 in achieving pure mode II failure. The authors also stated that the accuracy achieved by design criterion 2 is sometimes satisfactory for practical applications, which does not make its use prohibiting.

The strain energy release rate (SERR) is pursued to obtain the fracture toughness at crack initiation and crack propagation, and to characterize the R-curve behavior. Normally the SERR can be calculated by the conventional compliance calibration (CCM) method where the function between the specimen compliance and the crack length can be evaluated for various short crack lengths in experiments with stationary crack. The dependency of the crack length on the compliance of the specimen is then used in the crack propagation experiment to estimate the crack length by extrapolation. As such, the CCM assumes that no damage other than propagation of the debonding crack is developing during the experiment. Such condition is difficult to accomplish in cases where yielding of metals can occur in bi-material tests. Additionally, it was found that CCM cannot be used for the mode partitioning of mixed-mode results as in the case for the asymmetric and layered joint configuration [35]. An alternative called the extended global method (EGM) based on the beam theory [36] was used for more successful SERR calculation and mode partitioning in bi-material interfacial tests [35,37–39]. In the reported studies, the crack tip was visually observed using marked vertical lines or cameras, which may not be accurate and could be less suitable in cases where the adhesive layer is negligibly thin or completely absent, as in the directly wet-laminated composite-steel interfaces studied here. Moreover, the crack tip opening displacement (CTOD) cannot be measured by such visual observation.

In fracture problems involving composite-metal bi-material interfaces, where the size of the fracture process zone (FPZ) is non-negligible due to the plasticity of adherends resulting from micro-cracking of resin and fiber bridging, LEFM cannot be appropriately applied for fracture analysis. The non-linear interface behavior can be approximated with the help of cohesive zone modeling (CZM) where the constitutive behavior of the FPZ is defined by the traction-separation law derived from laboratory tests. The CZM has been extensively applied in the numerical simulation of delamination in composites [35,39–43]. Unfortunately, there is limited research [44] on the application of cohesive zone models for simulating the behavior of composite-steel bonded interface. The shape of

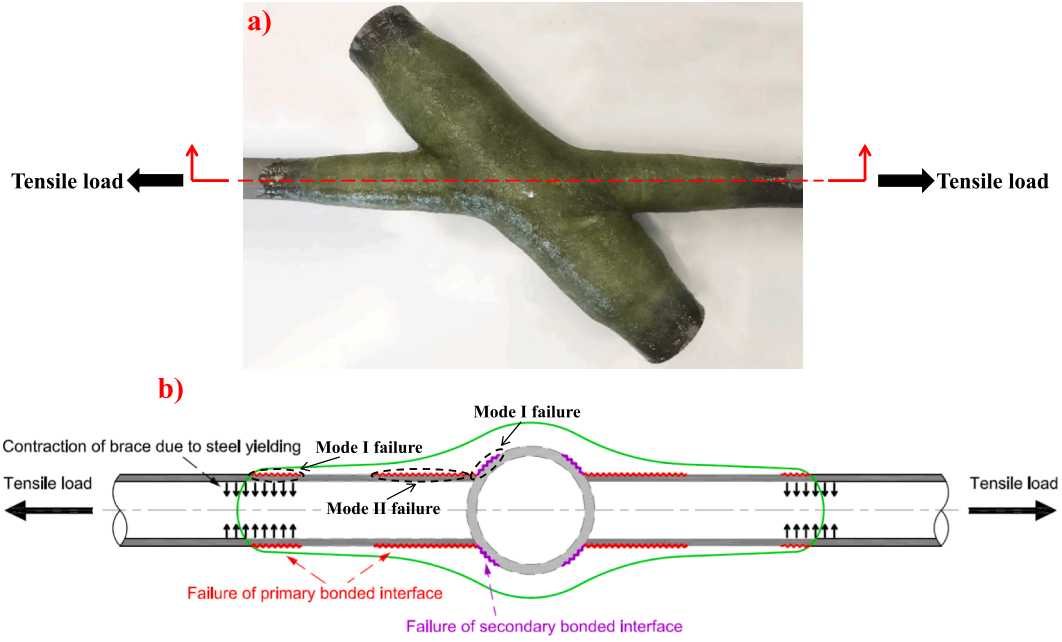

Fig. 1. A) wrapped composite joints – a 45° X-joint specimen; b) summary of failure modes and load transfer mechanism of wrapped composite joints loaded in tension [2].

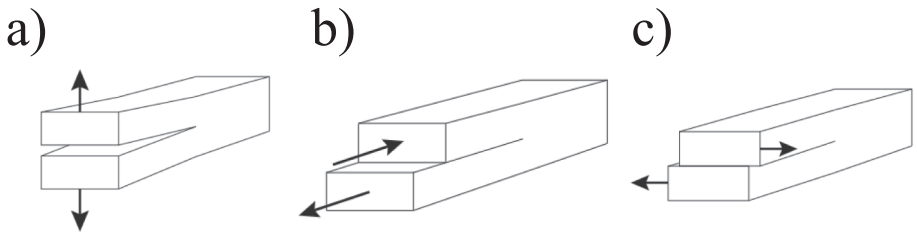

Fig. 2. Fracture modes of the interfacial cracking – a) mode I: opening; b) mode II: in-plane shear; c) mode III: out-of-plane shear.

the cohesive law is highly dependent on the material properties, composite layup, adherend surface treatment, etc. To the best of the authors' knowledge, there are basically three methods to determine the cohesive law:

1) The phenomenological approach, where the shape of the traction-separation law is predefined based on the plausible physical behavior at the cohesive interface and current literature. The cohesive law is validated using experimental results [35,39–43];
2) The direct method, in which the cohesive law is obtained by differentiating the strain energy release rate over CTOD directly measured from experiments [45–51];
3) The beam theory with bending rotations (BTBR) method, where CTOD is determined as a function of the equivalent crack advance, and the strain energy release rate as a function of the crack advance is determined using only the load and displacement data obtained from the test machine [52,53].

Methods 2 and 3 do not require assumptions of the shape of the cohesive law. However, these two methods are based on the path independent *J*-integral [54], primarily used for characterizing interlaminar failure. They require substantial adaptation for application to bi-material interfaces, particularly composite-steel interface where the yielding of steel is also present.

The research presented in this paper focused on acquiring the mode II fracture behavior of the glass fiber composite-steel bonded interface through testing and modeling of 3ENF and 4ENF specimen configurations. Such bonded interface is utilized in the innovative non-welded wrapped composite joints. The developed results and methods are also applicable to other connections where composite is directly bonded to steel (excluding adhesive) by wet lamination or other suitable application techniques. A novel approach was developed to analyze 2D DIC measurement data, enabling the determination of both the crack length and the crack tip opening displacement during the tests. The SERR was calculated by EGM from experiments and a four-linear traction-separation law was developed to simulate the mode II failure process by CZM in the FE model of the ENF experiments. The fracture process was clarified, and the DIC measurement method as well as the cohesive law were validated by good matches observed between testing and simulation results.

2. Experimental work

2.1. Specimens and materials

Three series of 3ENF and 4ENF tests summarized in Table 1 are performed to characterize and quantify the mode II fracture behavior of the composite-steel bonded interface, and the corresponding configurations of the tested specimens are illustrated in Fig. 3. 3ENF specimens with composite laminate positioned as the upper and the lower adherends are illustrated in Fig. 3a) and b) and tested in test series 1 and test series 2, respectively, to study the influence of adherend position on the mode II behavior of composite-steel bonded interface. 4ENF specimens illustrated in Fig. 3c) with composite laminate served as lower adherend (with respect to direction of the applied load) are tested in test series 3 to investigate the effect of a different loading scenario on the mode II fracture process of composite-steel bonded interface. Each test series is accomplished with at least 3 nominally identical specimens. The naming convention of the tested specimens refers to the testing method (3ENF/4ENF), position of the composite laminate (CU, CL – composite

Table 1
Overview of test series and dimensions of 3ENF and 4ENF specimens (unit: mm).

Test series	Specimens	h_{steel} (thickness of steel adherend)	$h_{composite}$ (thickness of composite adherend)	l (Specimen length)	$2L$ (span length)	B (Specimen width)	d (Distance between loading points)	a_0 (pre-crack length)
1	3ENF-CU-S1/2/3/4/5	4	12.3	220	180	25	–	30
2	3ENF-CL-S1/2/3	4	12.3	220	180	25	–	30
3	4ENF-CL-S1/2/3*	3	7.6	180	120	20	70	40

*The 4ENF specimens were produced with higher roughness of steel adherend, aiming to increase the bonding properties.

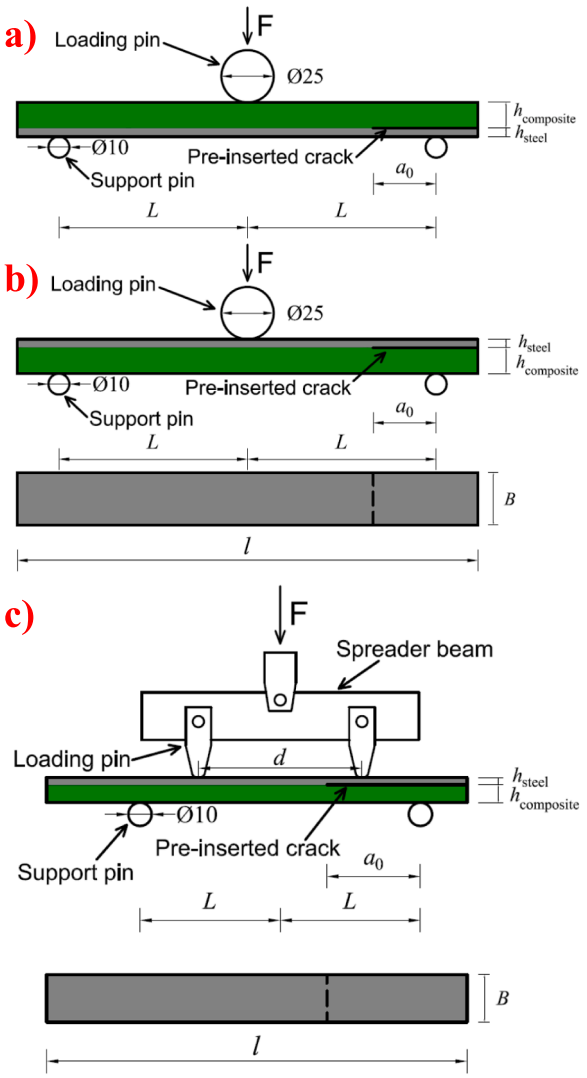

Fig. 3. Composite-steel mode II fracture test specimens: a) 3ENF specimens with composite as upper adherend; b) 3ENF specimens with composites as lower adherend; c) 4ENF specimens with composite as lower adherend.

laminate served as upper or lower adherend, respectively), and the specimen number (S1/2/3/etc.).

Overview of the dimensions of the test specimens are shown in Table 1. h_{steel} and $h_{composite}$ refer to the thickness of steel and composite laminate adherends, respectively, while the specimen length, specimen width and the span length are designated as l, B and $2L$, respectively, see Fig. 3. The pre-crack length a_0 is defined as the distance between the support roller (pin) and the pre-crack tip while the distance of the two loading pins in 4ENF specimens is designated as d. The 3ENF (test series 1 and 2) and 4ENF specimens (test series 3) were produced in 2 different batches. 3ENF specimens were produced first with low roughness of steel adherend, quantified by the root mean square roughness $Sq = 14$. Subsequently, 4ENF specimens were designed with decreased thickness of steel adherend and were produced with higher roughness of steel adherend ($Sq = 22$), aiming to increase the bonding properties. In 4ENF tests, the mode II crack is initiated by the shear strains at the crack which are proportional to the difference in longitudinal strains at the interface in the steel and composite adherends. Both adherends follow the same curvature due to bending. Therefore, decreasing the thickness of steel adherend relative to the thickness of the composite adherend helps reduce the longitudinal strain in the steel adherend at the crack tip, thereby reducing yielding of steel during crack initiation and propagation. It should be noted that the pre-crack length in the 3ENF test differs from the length used in the 4ENF test. The aim is to investigate the influence of the pre-crack length to half-span ratio (a_0/L) on the stability of crack propagation in the 3ENF test. A 30-mm pre-crack length was used in test series 2 with a_0/L=0.33. Subsequently, a_0 was increased to 63 mm (a_0/L=0.7) as recommended by the literature in the additional 3ENF tests in section 6.2 to promote stable crack propagation. In the 4ENF test, a_0 = 40 mm was chosen based on previous experience, which typically leads to stable crack propagation.

The composite-steel bonded plates were manufactured by hand-lamination in a wet-layup process. Test coupons were cut from the

laminated composite-steel plates using water jet. Surface treatment of the steel plate, grade S355, included grit blasting and degreasing by acetone. A non-adhesive Teflon based tape with 32 μm thickness was placed at the steel plate end before lamination to create a pre-crack. Subsequently, the hand lay-up lamination was performed using E-glass fiber plies and a vinyl ester thermoset resin in a controlled factory environment at room temperature (20–23 °C) and humidity (48–53 % RH) conditions with quality control to ensure good compaction and avoiding air gaps, see Fig. 4. The E-glass fiber plies are composed of bidirectional woven fabrics and chopped strand mat, and the composite laminate presents a fiber volumetric fraction ranging 30–32 %. The laminated plate was left for curing in a controlled environment of temperature and humidity, and no post-curing was applied. It should be noted that the composite laminate was directly bonded on the steel plate without application of intermediate adhesive layer so that the thickness of the adhesive layer was negligible. Mechanical properties of the composite and steel adherends were measured by composite and steel coupon experiments (see Fig. 5) following the standard testing methods and are presented in Table 2.

2.2. Experiment and measurement set-up

The 3ENF and 4ENF tests were conducted in the UTM 25 universal testing machine with a 15 kN load cell, as shown in Fig. 6. The specimens remained supported on the test frame and were connected to the fixture through either one cylindrical loading pin in 3ENF tests or two arc-edged loading pins symmetrically bolted connected to a spreader beam in 4ENF tests. The crack driving force F was applied through the hydraulic jack to the upper adherend at a constant displacement rate of 1 mm/min. Prior to the tests, the specimens were coated on the side to measure the full field displacements around the crack path using a 2-dimensional (2D) digital image correlation (DIC) system. A thin layer of white matt paint was coated to the side surface of the specimens followed by a sprayed black speckle pattern to create the measurement surface for DIC analysis. A camera with 51-megapixel resolution was set to take photos of the specimens at a frequency 1/3 Hz and a polarized blue light was used during the test to provide steady illumination conditions for accurate measurements. A calibration block with a length of 30 mm was placed on the specimen to provide a reference length for the DIC measurements, as shown in Fig. 7. After the tests, the photos were imported into the GOM Correlate Pro software to track and measure the deformation of the specimens based on the surface component built at the reference stage, see Fig. 7.

3. Finite element modeling (FEM)

The fracture behavior of 3ENF and 4ENF specimens was simulated by the 3D FE models in ABAQUS in the quasi-static manner using the explicit solver [60], due to its advantages in computation convergence and dealing with non-linear behavior such as contact problems. Mass scaling method was conducted with definition of smooth step function to increase the computational efficiency. Fig. 8a) and b) show the boundary conditions applied in the 3ENF model and the 4ENF model, respectively. The loading pin and the support pin were modeled by the cylindrical shell to simulate the sliding between the pins and the specimens due to deflection of the latter observed during the experiments. The outer surfaces of the loading pin and the support pins were kinematically constrained to the “Load” and the “hold” reference points in all degrees of freedom, respectively, see Fig. 8a) and b). The load in the model was applied through negative displacement in vertical direction (U2) to the reference point “load” which is fixed in translation in global X and Z direction and rotation in global X and Y direction. In the 4ENF model the translation in global X direction was released at the reference point “load” to allow the translational movement of the spreader beam observed in the experiments. All degrees of freedom were fixed at the reference point “Hold” to replicate the constraints during the tests.

The global mesh size of the specimens was 2 mm according to the mesh sensitivity analysis in the joint modeling which is not included in this paper. Linear element was used to save computational cost without sacrificing the simulation accuracy, considering the relatively fine mesh size. The composite adherend was modelled using the 4-node tetrahedral solid element (C3D4), see Fig. 8c), attributed to its advantages in simulating stresses and strains in the through-thickness direction and in meshing composite laminate

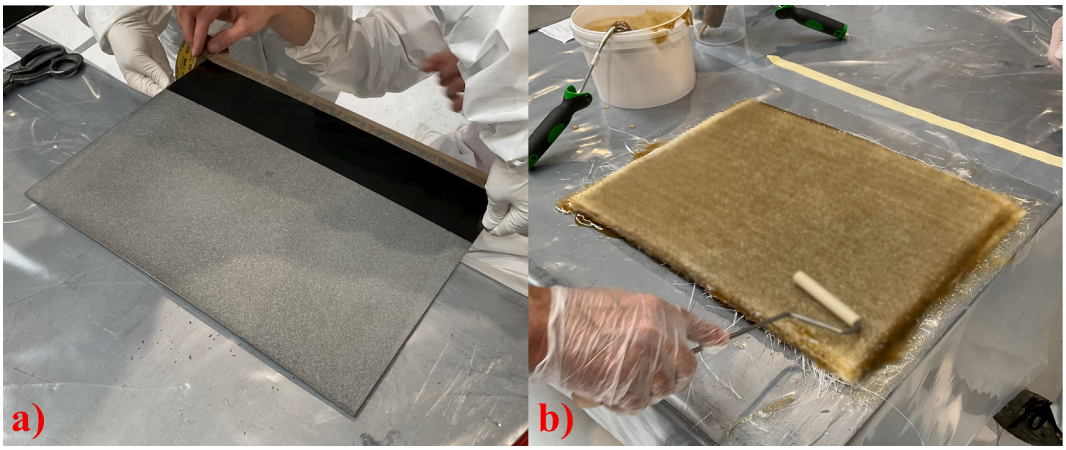

Fig. 4. Manufacturing of the composite-steel bonded plate: a) the steel plate with a pre-insert; b) the hand lay-up lamination process.

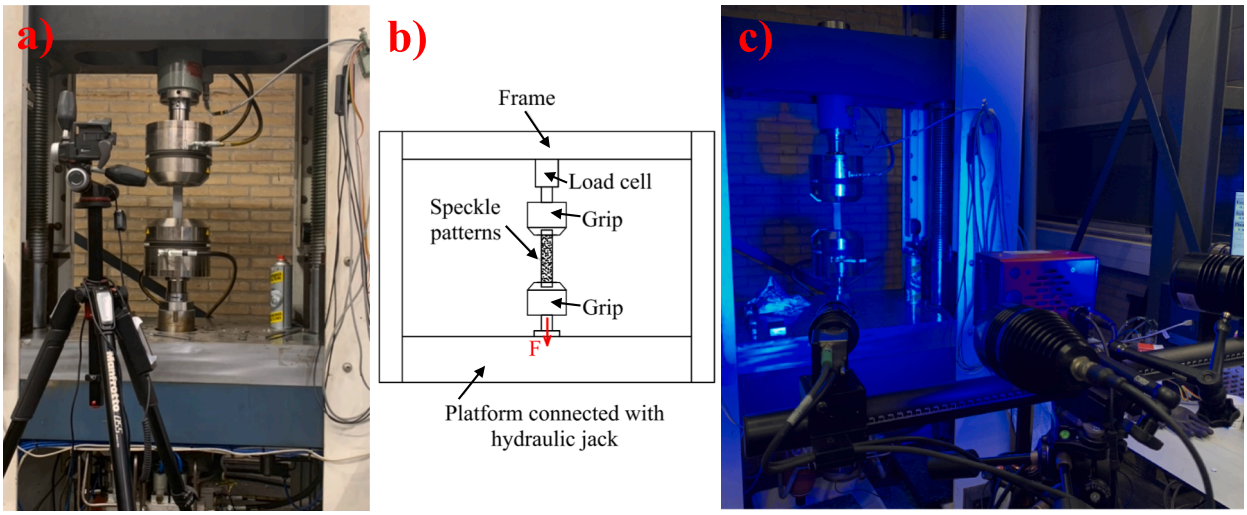

Fig. 5. Steel and composite coupon experiments conducted in a) the Instron 1251 tensile and compressive press with a schematic view in b); c) the 3D-DIC measurement system used during the coupon experiments.

Table 2
Mechanical properties of the steel and composite adherends.

Material	Mechanical properties	Average value (and CoV [%])	Standard
Steel	Tensile modulus – E	210000 N/mm^2 (5.74)	ISO 6892–1[55]
	Yield strength – σ_e	360.91 MPa (4.86)	
Composite	In-plane tensile modulus in x/y direction – $E_{x,t} = E_{y,t}$	11798 N/mm^2 (6.37)	ISO 527–1[56] and 527–2[57]
	In-plane tensile strength in x/y direction – $f_{x,t} = f_{y,t}$	216 MPa (5.78)	
	In-plane compressive modulus in x/y direction – $E_{x,c} = E_{y,c}$	12077 N/mm^2 (4.50)	ISO 14,126[58]
	In-plane compressive strength in x/y direction – $f_{x,c} = f_{y,c}$	200 MPa (3.79)	
	In-plane shear modulus – G_{xy}	3120 N/mm^2 (6.81)	ISO 14,129[59]
	In-plane shear strength – $f_{xy,v}$	72.2 MPa (2.59)	

with curved and complex geometry. The steel adherend was meshed with 8-node hexahedral element (C3D8R) and 4 elements were meshed in the through-thickness direction to accurately simulate the bending-dominated deformation. The engineering constants were used to simulate elastic modulus of composite in the orthotropic direction using the material properties from coupon experiments, as summarized in Table 2. In addition, the elastic modulus in through-thickness tensile and shear behavior is $E_3 = 5000$ N/mm^2 and $G_{13} = G_{23} = 2500$ N/mm^2, respectively. These values were obtained based on the manufacture data and calculation using classical laminate theory and rule of mixture.

The cohesive contact approach was used to model the bonding of the composite-steel interface, as shown in Fig. 8a) and b). This approach is primarily intended for situations where the adhesive layer thickness is negligible and is easier to define compared to cohesive elements. The cohesive zone model (CZM) was assigned to the contact surface pairs with introduction of the traction-separation law to describe the fracture behavior in between. The traction-separation law was implemented in ABAQUS software using the tabular input provided in its graphical user interface. This tabular input allowed us to define the relationship between the interface damage variable and the effective crack tip opening displacement (CTOD) according to the certain geometry of the traction-separation law. The damage variable was calculated by considering the stiffness of the interface, which was also included in the ABAQUS input with a value of 10000 N/mm^3. The damage variable remains equal to 0 until the effective CTOD reaches the value corresponding to the stage of crack initiation. Based on the experimental and numerical results of 3ENF and 4ENF specimens, a four-linear traction-separation law was proposed to replicate mode II fracture process of composite-steel bonded interface which will be explained thoroughly in section 4.

4. Mode II fracture process represented by a four-linear traction-separation law

Due to existence of fiber bridging, the fracture process of the composite-steel bonded interface does not follow the assumption of LEFM. On the contrary, the non-linear behavior near or around the interface, with the fracture process zone (FPZ) encompassing various stages of fracture process development, is formed as shown in Fig. 9a).The relation between the traction and the crack tip opening displacement (CTOD) of the (pre) crack tip within the FPZ is defined here by a four-linear traction-separation law, as illustrated in Fig. 9b). Such set-up of the traction-separation law is explained here through physics-based considerations and assumptions.

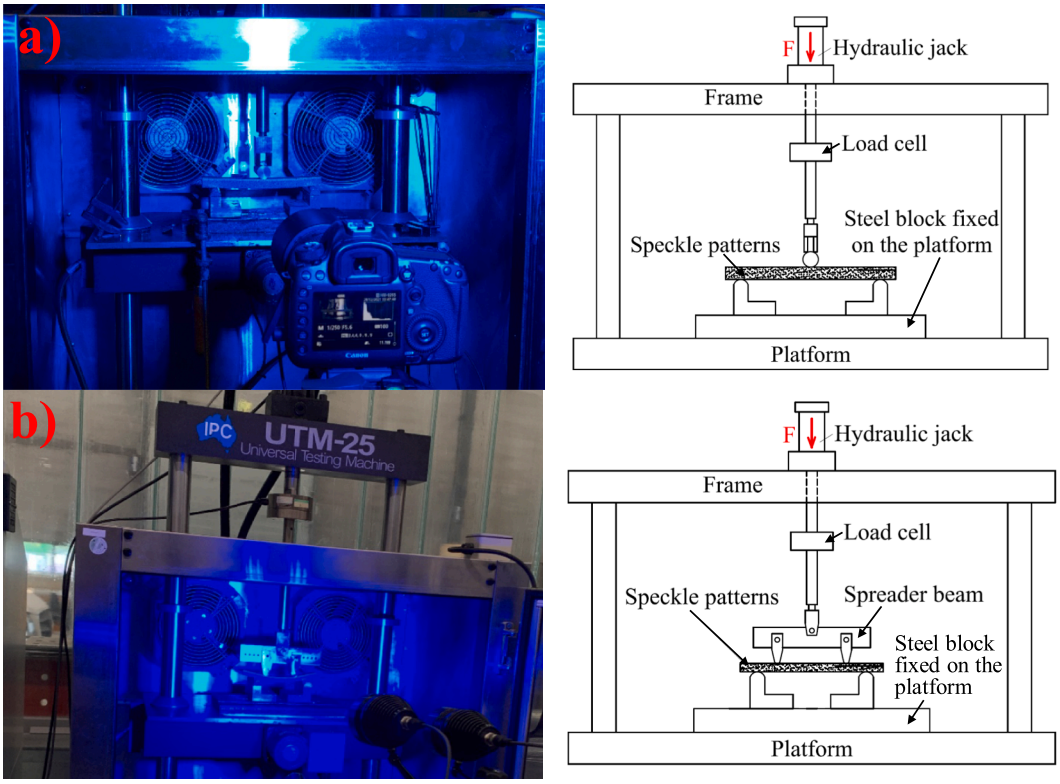

Fig. 6. The set-up of a) 3ENF and b) 4ENF test.

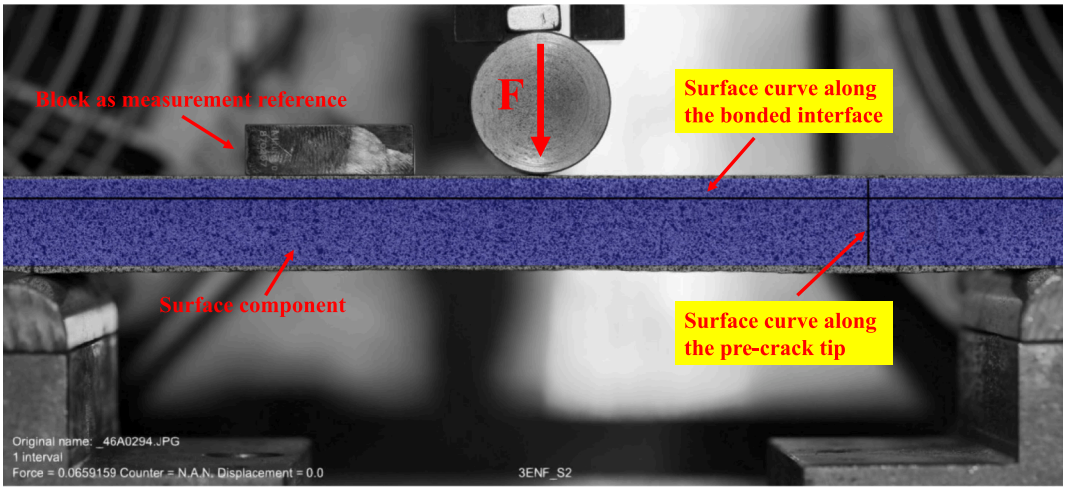

Fig. 7. DIC analysis in GOM Correlate Pro software – a 3ENF specimen as an example.

The interface model is then phenomenologically validated in the follow-up sections through detailed comparison of global and local behavior in the ENF experiments and FE analysis, by looking at load–displacement response, crack propagation and CTOD progression. Four critical stages are defined for further explanation: "p" – onset of plasticity; "c" – onset of cracking; "b" – onset of fiber bridging; "f" – failure. Two out of three distinct phenomena described in the fracture process are consistent to the current literature [41,45,46]: phenomenon 1 – crack tip deformation and phenomenon 3 – fiber bridging, indicated by orange and blue regions in Fig. 9b), respectively. In addition, phenomenon 2, defined here as softening, is introduced in between to consider the contribution of mechanical interlocking of the resin embedded in the rough steel surface.

In the beginning of the fracture process, the cohesive traction increases linearly until reaching σ_p at stage "p", referring to onset of plasticity, where the traction increases at a slower pace due to plastic deformation and micro-fracture of the resin until reaching σ_c at

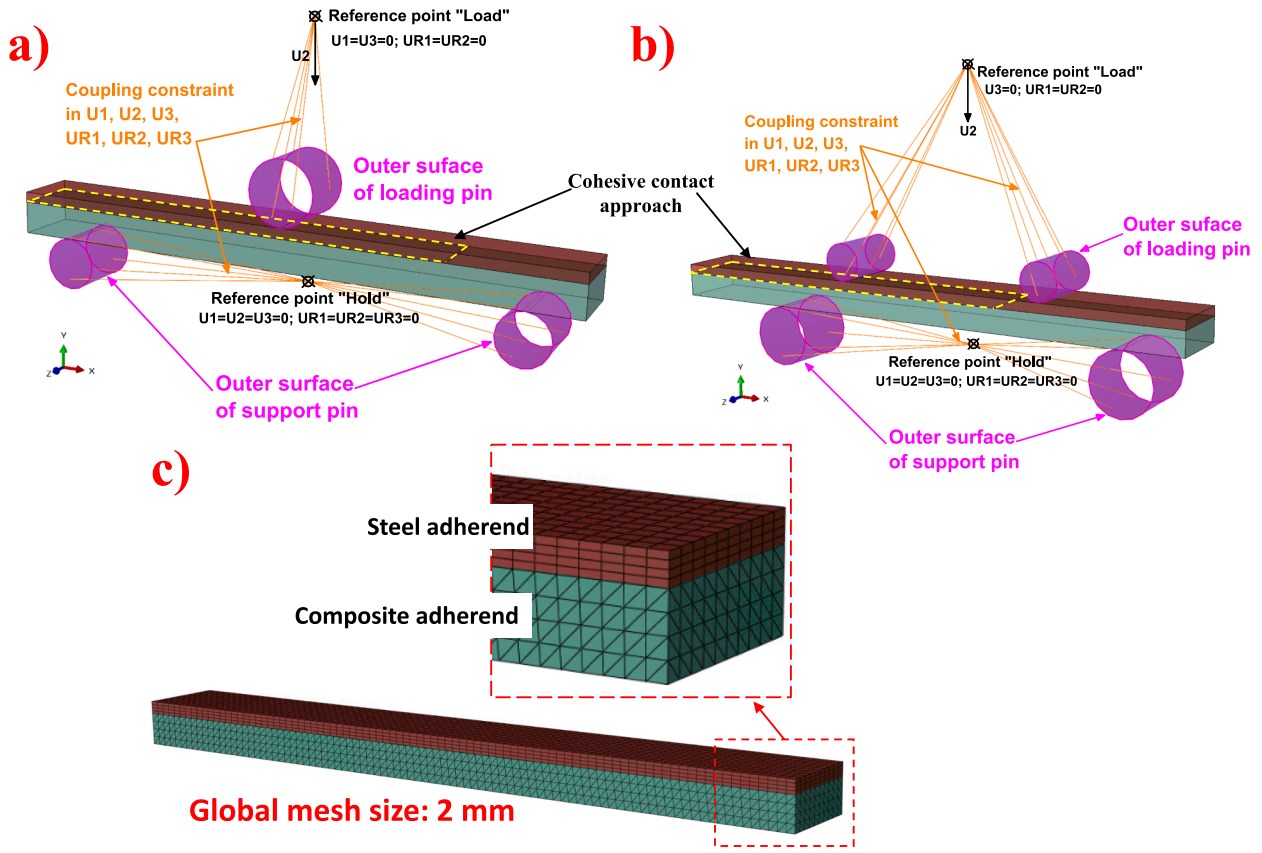

Fig. 8. Boundary conditions of a) 3ENF FE model and b) 4ENF FE model, and c) mesh overview of the specimens.

stage "c", corresponding to onset of cracking. The SERR dissipated to reach stage "c" (the orange area) is defined as the critical SERR for crack initiation or crack tip fracture resistance [41,45,46] with the symbol $G_{IIc,}$tip. The distance between point at stage "p" and point at stage "c" on the interface (see the detail cut-out in Fig. 9a) is defined as the FPZ length related to crack initiation designated as $FPZ_{IIc,tip}$. Subsequently, the traction is assumed to remain constant ($\sigma_c = \sigma_b$) as the CTOD increases until stage "b", hypothetically attributed to pull-out of resin from valleys in the micro profile of steel surface roughness. Engaging such mechanical interlocking load transfer between steel and composite contact surfaces provides a significant amount of toughness in mode II fracture. The SERR dissipated from stage "c" to stage "b" is defined as the SERR due to softening (the green area) with the symbol of $G_{II,soft}$. The distance between point at stage "c" and point at stage "b" on the interface is defined as the FPZ length related to softening designated as $FPZ_{II,soft}$. Aligned with the current literature dealing with mode I fracture behaviour [41,42], $G_{II,soft}$ and $FPZ_{II,soft}$ should be considered as part of $G_{IIc,tip}$ and $FPZ_{IIc,tip}$, respectively. This is because of negligible contribution of the softening phenomenon to the fracture toughness due to weak mechanical interlocking, i.e. pull-out resistance, in the mode I behavior. Contrarily, as noticed by the large fracture toughness in the mode II experiments, contribution of softening phenomenon is suspected to be significant and distinct in mode II fracture process. Therefore, $G_{II,soft}$ and $FPZ_{II,soft}$ is proposed in such tri-staged model, opposed to usually considered dual-stage model including initiation and fiber bridging behavior only. The softening is followed by fiber bridging where the traction values decrease gradually from σ_b at stage "b" to 0 at stage "f", and the corresponding SERR dissipated is defined as the SERR corresponding to fiber bridging with the symbol of $G_{II,br}$ (the blue area). The distance between point at stage "b" and point at stage "f" on the interface is defined as the FPZ length related to fiber bridging designated as $FPZ_{II,br}$. When stage "f" is reached, the fracture surface is completely separated at the pre-crack tip and the SERR attains a constant value in an R-curve referred to as the critical SERR for crack propagation or steady state fracture resistance [42,45,46] designated as G_{IIc}. The distance between points at stage "p" and at point at stage "f" on the interface is defined as the FPZ length related to crack propagation designated as FPZ_{IIc}. The critical SERR for crack propagation and total length of the fracture process zone based on Fig. 9 are defined as:

$$G_{IIc} = G_{IIc,tip} + G_{II,soft} + G_{II,br} \tag{1}$$

$$FPZ_{IIc} = FPZ_{IIc,tip} + FPZ_{II,soft} + FPZ_{II,br} \tag{2}$$

The area underneath the traction-separation law in Fig. 9 corresponding to $G_{II,soft}$ and the associated length $FPZ_{II,soft}$ are indicated largest, based on the test results, indicating that softening phenomenon provides the majority of the resistance to the bonded interface

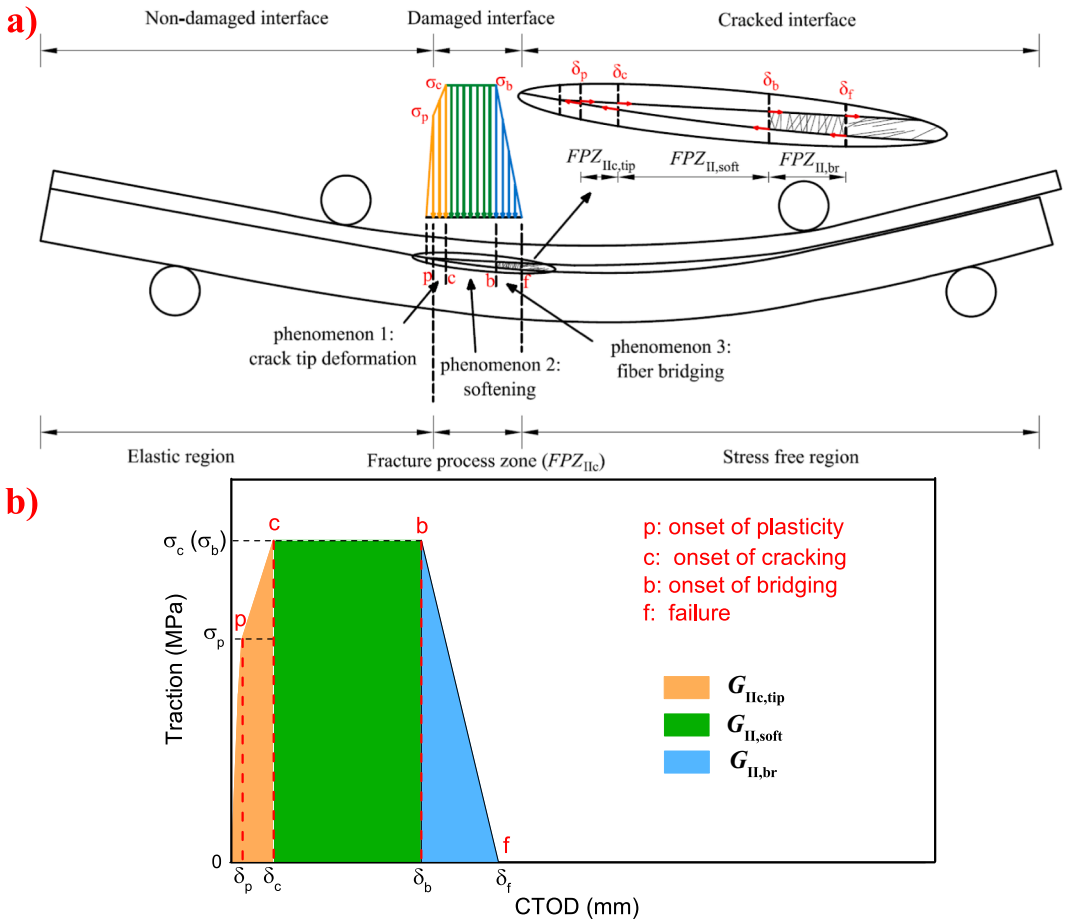

Fig. 9. A) scheme of mode ii fracture process of composite-steel bonded interface – 4enf specimen as an example; b) four-linear traction-separation law to describe the mode ii fracture process.

in mode II fracture. The values in terms of CTOD, and corresponding tractions at the critical stages ("p", "c", "b" and "f") as well as values of the critical SERR ($G_{IIc,tip}$ and G_{IIc}) used in the defined cohesive laws in the 3ENF and 4ENF modeling are summarized in Table 3. The values are obtained based on the average values of the acquired test results which will be detailed in the follow-up sections. The main difference observed is that the cohesive law applied in modeling 4ENF tests demonstrates more pronounced softening and fiber bridging behavior compared to that used in modeling 3ENF tests. It should be noted that this difference is attributed to variations in steel roughness and bonding properties in the two different batches and not necessarily due to difference of fracture test and characterization methodology in those two types of tests. 4ENF specimens were manufactured with higher steel roughness, resulting in increased fracture toughness.

It should be noted that the cohesive law can also be obtained by the inverse method using only the load and displacement data obtained from the test machine [52,53]. However, currently it is mainly used for the characterization of interlaminar failure and requires further development to be used in the bi-material interface, especially the composite-steel interface where the yielding of steel is also present.

Table 3
Parameters of the four-linear cohesive laws used in modeling 3ENF and 4ENF test.

Modeling scenario	Stage	Onset of plasticity – stage "p"		Onset of cracking – stage "c"		Onset of fiber bridging – stage "b"		Failure – stage "f"		Critical SERR	
	Symbols	δ_p (mm)	σ_p (MPa)	δ_c (mm)	σ_c (MPa)	δ_b (mm)	σ_b (MPa)	δ_f (mm)	σ_f (MPa)	$G_{IIc,tip}$ (N/mm)	G_{IIc} (N/mm)
3ENF	Values	0.0015	14.7	0.031	22	0.089	22	0.096	0	0.56	1.9
4ENF	Values	0.002	20	0.037	30	0.116	30	0.259	0	0.89	5.4

5. Fracture data analysis

5.1. Determination of critical stages in mode II fracture process

The method to determine critical stages in 3ENF and 4ENF tests is explained in Fig. 10 using specimen 4ENF-CL-S1 as an example. The load–displacement curve (in red) of the specimen is compared to the variation of its tangential stiffness, the variation of crack length and the variation of CTOD, in Fig. 10a), b), and c), respectively. These variations are plotted against the applied displacement (the orange curves). It can be seen that stage "p", stage "c" and stage "f" refer to the turning points where decreasing rate of tangential stiffness grows suddenly and meanwhile increasing rate of crack length a and rate of CTOD rises instantly. Stage "p" cannot be determined through observing the increasing rate of crack length a, as it starts to grow after stage "c". However, it can be determined by good agreement between variations of tangential stiffness and CTOD. It should be noted in Fig. 10 that this method helps determine stage "f" but does not allow for the identification of stage "b" in 4ENF tests. This is because there is no sudden increase of crack length or CTOD after stage "b", attributed to stable crack growth. On the contrary, this method helps determine stage "b" but cannot identify stage "f" in 3ENF tests because the specimens fail immediately after stage "b" without reaching stage "f" attributed to unstable crack growth, see Fig. 19–Fig. 21. Therefore, it can be beneficial to perform both types of tests to better characterize all the stages in the 4-linear traction-separation law.

In FEM the critical stages were easily determined by inspecting the output variable CSDMG (the scalar damage variable of the bonded interface) at the pre-crack tip based on the input values.

5.2. Shear strain based DIC method to determine the crack length and the CTOD

In 3ENF and 4ENF tests the crack length a and the CTOD were determined by analysis of DIC measurement data in GOM Correlate Pro software. It should be noted that these two parameters cannot be explicitly measured in 3ENF and 4ENF tests where the direction of the crack opening is parallel to the direction of crack extension. Instead, a new "shear strain scaling method" was proposed here to measure the crack length a. It involves building a surface curve along the composite-steel bonded interface (see Fig. 7) and reading the shear strain from the surface curve data (see Fig. 11). It can be inferred from the extended global method (EGM) [31,32] that the significant increase in shear strain from the crack tip to the right support point along the interface is caused by the difference of maximum tensile and compressive strains in the upper and lower adherend, respectively. Therefore, the present crack tip can be determined indirectly by observing local increase of shear strains along the bonded interface. To eliminate interference of elastic deformation in shear strain increase and to ensure accuracy in defining the curve path directly on the interface, the shear strains at a

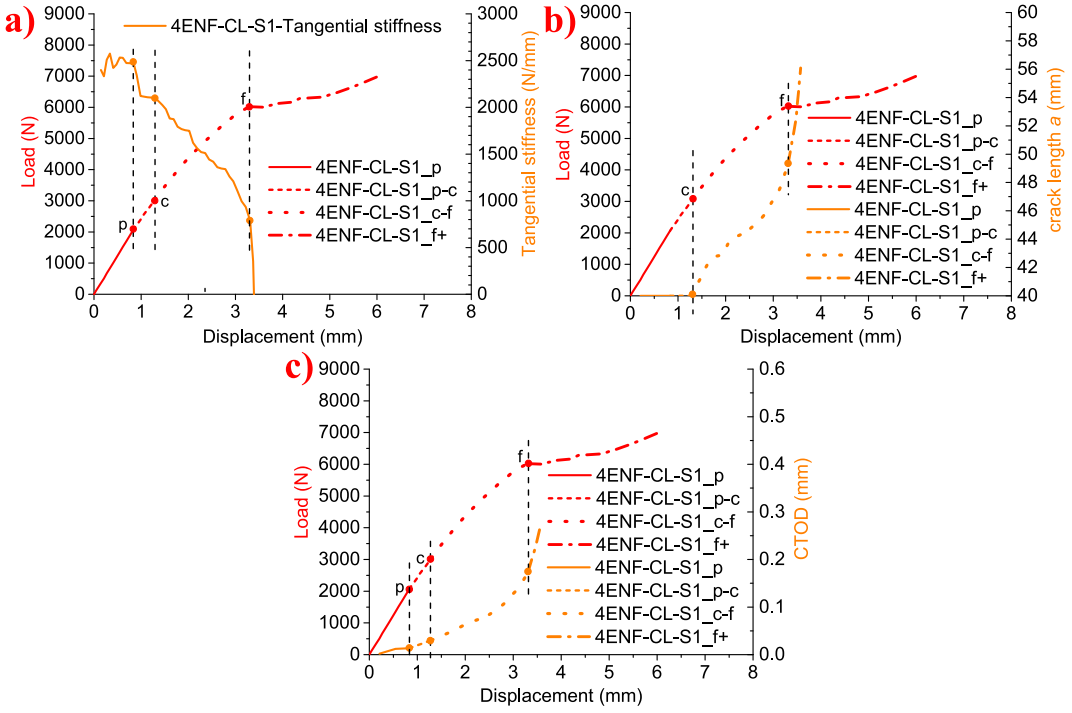

Fig. 10. Illustration of the method to determine critical stages in experiments through a) tangential stiffness, b) crack length a and c) CTOD – an example of specimen 4ENF-CL-S1 (p, p-c, c-f, f + indicates elastic behavior until stage "p", stage "p" to stage "c", stage "c" to stage "f", after stage "f", respectively).

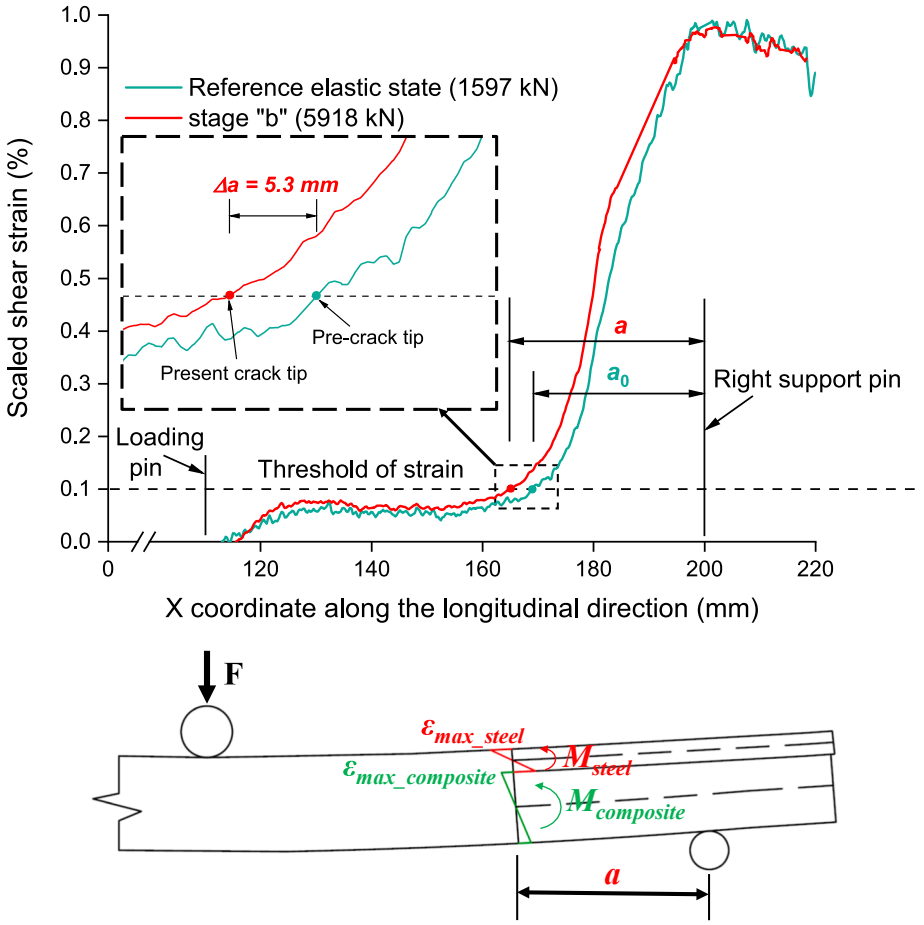

Fig. 11. Illustration of determination of crack length and growth in DIC using the shear strain scaling method – an example of specimen 3ENF-CL-S2.

later load state (the red curve) are relativized and scaled to shear strains that correspond to a selected reference elastic state (the green curve), as shown in Fig. 11. If there were no crack extension, the scaled shear strains at a later load state would be identical to the strains at the reference elastic state. The deviations from such an idealistic state were used to identify the present crack tip and quantify the crack length a using the strain threshold identified as 0.1 % by pinpointing at which strain level the shear strains significantly increase from a flat, steady, trend to a higher strain distribution trend. The strain threshold depends on the selected reference elastic

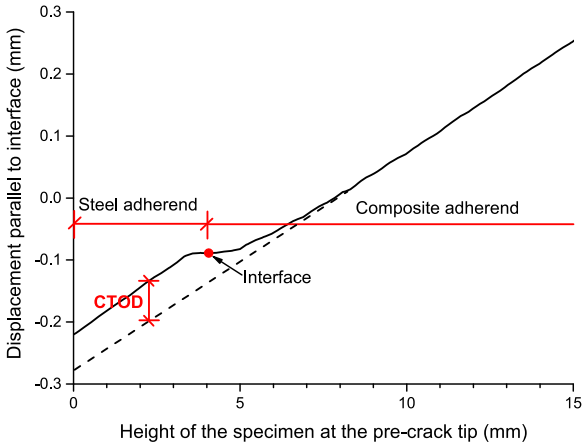

Fig. 12. Illustration of determination of mode II CTOD by DIC – an example of specimen 3ENF-CL-S2.

load level and specimen geometry, and therefore shall be determined for each specific test set-up and selected reference load level. In the present study the reference load level for scaling was kept the same.

The CTOD was quantified as well with the help of detailed DIC data. The proposed asymptotic analysis method involves analyzing the horizontal displacement distribution along the height of the specimens at the pre-crack tip as shown in Fig. 12, where the measurements of displacements are obtained from the vertical surface curve in Fig. 7. Two parallel straight lines were observed at the steel and composite adherend due to the elastic bending deformation. If there were no slip at the interface related to crack initiation, growth, and propagation, the two lines would overlap. Contrarily, once the fracture process starts, the CTOD is characterized by the displacement shift at the interface between the straight lines fitted to the regions on the upper (steel) and lower (composite) adherends away from the interface.

In the FEM, the present crack tip is determined as the location where the CSDMG just reaches the input values corresponding to stage "c" identified as crack initiation, as shown in the front of the yellow contour in Fig. 13. The CTOD is obtained by subtracting the displacement parallel to the interface from the interface surfaces of steel and composite adherend at the pre-crack tip.

5.3. Determination of SERR by EGM

The strain energy release rate (SERR) was calculated using the extended global method (EGM) [38,39] where the total SERR is:

$$G_{total} = \frac{6}{B^2}\left[\frac{M_{steel}^2}{E_{steel}h_{steel}^3} + \frac{M_{composite}^2}{E_{composite}h_{composite}^3} - \frac{\left(M_{steel}+M_{composite}\right)^2}{E\left(h_{steel}+h_{composite}\right)^3}\right] \tag{3}$$

where E_{steel}, I_{steel}, $E_{composite}$ and $I_{composite}$ are the elastic modulus, the moment of inertia in the section of the crack tip of the steel adherend and composite adherend, respectively. E and I are the equivalent elastic modulus and the equivalent moment of inertia of the specimen at the crack tip, respectively. B, h_{steel} and $h_{\text{composite}}$ are the width of the specimen, the height of steel and composite adherends, respectively, see Fig. 3. M_{steel} and $M_{composite}$ are the bending moments (assumed positive when counterclockwise) of the steel and composite adherends at the crack tip, respectively. The design of 3ENF and 4ENF specimens in this study did not satisfy the longitudinal strain based criterion [61], so the equivalent longitudinal strain ratio of the steel and composite adherends was introduced to guarantee pure mode II in mode partitioning of bi-material bonded joints [37]:

$$\beta = \frac{E_{composite}h_{composite}^2}{E_{steel}h_{steel}^2} \tag{4}$$

The applied moments can be resolved as:

$$M_{steel} = M_{\text{I}} + M_{\text{II}} \tag{5}$$

$$M_{composite} = -\beta M_{\text{I}} + \psi M_{\text{II}} \tag{6}$$

where ψ is defined as the bending stiffness ratio of steel and composite adherends to assure the identical curvature in the two adherends to obtain pure mode II:

$$\psi = \frac{E_{composite}I_{composite}}{E_{steel}I_{steel}} \tag{7}$$

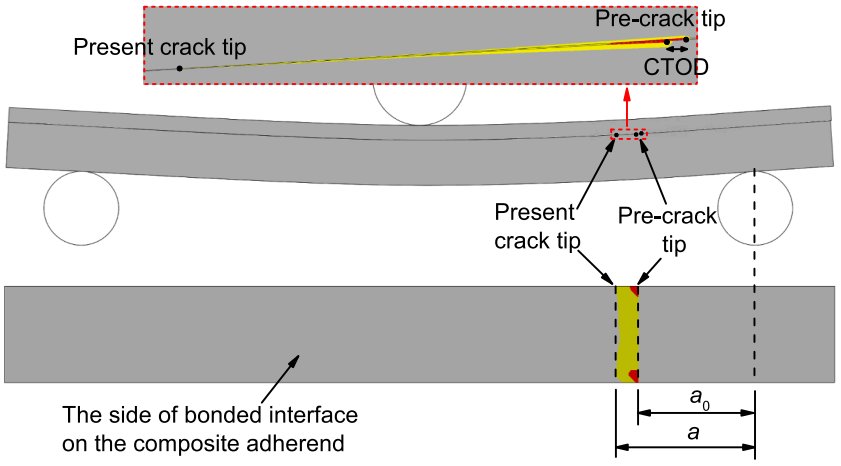

Fig. 13. Illustration of determination of a and CTOD in FEM – an example of 3ENF modeling.

Substitution of Equation (5) and Equation (6) into Equation (3) leads to the mode partition of G_{total} into G_{II} as:

$$G_{II} = \frac{\left(\beta M_{steel} + M_{composite}\right)^2}{2B(\beta+\psi)^2}\left(\frac{\psi+1}{E_{steel}I_{steel}} - \frac{(\psi+1)^2}{EI}\right) \tag{8}$$

EI is the equivalent bending stiffness of the specimen and is calculated as:

$$EI = E_{steel}I_{steel} + E_{composite}I_{composite} + E_{steel}A_{steel}(z - z_{steel})^2 + E_{composite}A_{composite}(z - z_{composite})^2 \tag{9}$$

where A_{steel}, z_{steel}, $A_{composite}$, $z_{composite}$ are the cross-section areas and the z coordinates of the centroids of the steel and the composite adherends, respectively. z is the coordinate of the equivalent centroid of the specimen cross-section.In the present 3ENF tests, M_{steel} and $M_{composite}$ are calculated as:

$$M_{steel} = \frac{FaE_{steel}I_{steel}}{2(E_{steel}I_{steel} + E_{composite}I_{composite})} \tag{10}$$

$$M_{composite} = \frac{FaE_{composite}I_{composite}}{2(E_{steel}I_{steel} + E_{composite}I_{composite})} \tag{11}$$

where the F is the applied load and a is the present crack length, respectively. Therefore, the SERR in mode II can be calculated as:

$$G_{II} = \frac{F^2a^2\left(\beta E_{steel}I_{steel} + E_{composite}I_{composite}\right)^2}{8B(\beta+\psi)^2\left(E_{steel}I_{steel} + E_{composite}I_{composite}\right)^2}\left(\frac{\psi+1}{E_{steel}I_{steel}} - \frac{(\psi+1)^2}{EI}\right) \tag{12}$$

In the presented 4ENF tests, M_{steel} and $M_{composite}$ are calculated as:

$$M_{steel} = \frac{F(2L-d)E_{steel}I_{steel}}{4\left(E_{steel}I_{steel} + E_{composite}I_{composite}\right)} \tag{13}$$

$$M_{composite} = \frac{F(2L-d)E_{composite}I_{composite}}{4\left(E_{steel}I_{steel} + E_{composite}I_{composite}\right)} \tag{14}$$

where F, L and d are the applied load, half span length, and the distance of the two loading pins, respectively. Therefore, the SERR in mode II can be calculated as:

$$G_{II} = \frac{F^2(2L-d)^2\left(\beta E_{steel}I_{steel} + E_{composite}I_{composite}\right)^2}{32B(\beta+\psi)^2\left(E_{steel}I_{steel} + E_{composite}I_{composite}\right)^2}\left(\frac{\psi+1}{E_{steel}I_{steel}} - \frac{(\psi+1)^2}{EI}\right) \tag{15}$$

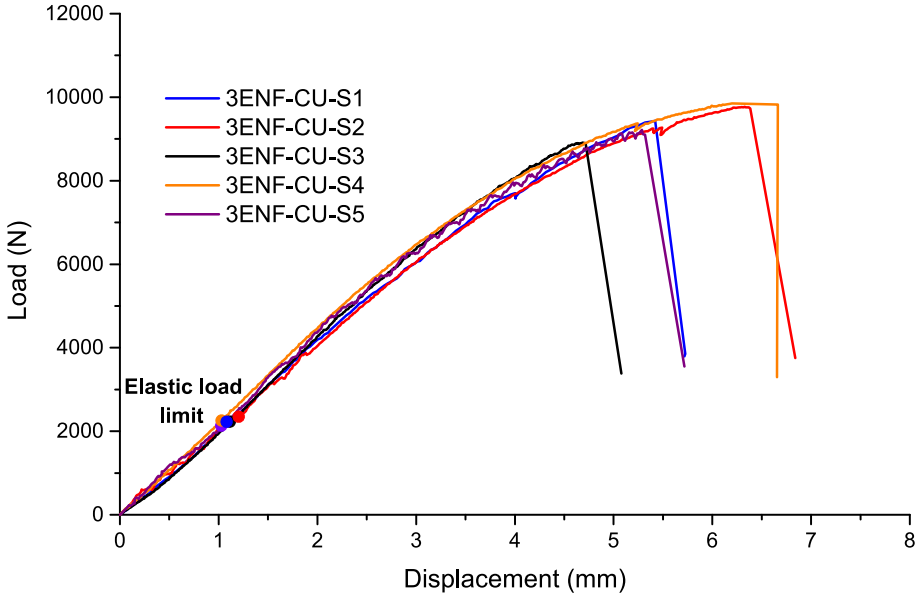

Fig. 14. Load-displacement response of 3ENF specimens tested with composite laminate as upper adherend.

6. Results and discussion

6.1. Test results of 3ENF specimens with composite laminate as upper adherend

The load–displacement curves of five 3ENF specimens tested with composite laminate as upper adherend are shown in Fig. 14. It shows that non-linearity occurred at approximately 2000 N while the ultimate resistance deviates within the range of 8000–10000 N. The elastic load limit is determined by analyzing the variations of tangential stiffness within load–displacement curves. It refers to the turning point where decreasing rate of the tangential stiffness grows suddenly for the first time. Fig. 15 shows the front view of a characteristic specimen 3ENF-CU-S5 during loading, and Fig. 16 illustrates its fracture morphology after test. It can be observed that the crack migrates from the composite-steel bonded interface to the inter-laminar failure plane in the composite adherend directly at the pre-crack tip, without initiation or propagation occurring along the bonded interface. The crack transition is attributed to micro cracking of the composite plies close to the bonded interface due to tensile bending when the composite laminate is positioned as the upper adherend. This transition of crack path helps improve the bonding behavior by allowing more energy dissipation but leads to difficulty in obtaining mode II fracture properties of the composite-steel bonded interface.

6.2. Test results of 3ENF specimens with composite laminate as lower adherend

To prevent crack migration from the bonded interface to the inter-laminar interface, the composite laminate adherend is positioned as the lower adherend in test series 2 and test series 3 (4ENF test). The aim is to keep composite plies close to the bonded interface in state of longitudinal compression due to the local arm bending moment. The assumption is that the longitudinal compression in combination with the through thickness shear is restraining more the crack development in the composite than the combination of longitudinal tension and through thickness shear. The load–displacement response of the 3ENF specimens in test series 2 is shown in Fig. 19 where the critical stages (“p”, “c” and “b”) are identified and the associated values of applied displacement and load are summarized in Table 4. The fracture morphology is shown in Fig. 17 which indicates that there is nearly no fiber bridging present on the debonded interface. This is due to lower steel roughness in the production batch of 3ENF specimens. More pronounced fiber bridging was observed in the 4ENF specimens produced with increased steel roughness. It can be seen from Fig. 19 that onset of plasticity (stage “p”) corresponds to the elastic load limit at approximately 2000 N followed by crack initiation at approximately 3500 N (stage “c”). Subsequently, softening leads to gradual increase of load until the peak load is reached at stage “b” within the load range of 5000–6000 N, where the bonded interface fails immediately with unstable crack propagation. There are two reasons accounting for the unstable crack propagation: 1) the bending moment at the present crack tip keeps increasing as the crack advances leading to consistently increasing SERR which is unfavourable for stable crack propagation; 2) fiber bridging is negligible on the fracture surface as shown in Fig. 17 such that the remaining resistance of the interface is too small to retain stable crack growth. The fracture morphology in Fig. 17 clearly shows that crack propagation happened merely on the bonded interface, therefore demonstrating the effectiveness of positioning composite laminate as the lower adherend in preventing crack transition in 3ENF test.

Fig. 20 and Fig. 21 illustrate the development of the crack length a and the CTOD at the pre-crack tip with the increased applied displacement during the tests, respectively. The pre-crack tip starts to open at stage “p”, but the opening displacement is limited (less than 0.02 mm) according to DIC measurements. After the crack is initiated at stage “c”, the crack length and the crack opening develop steadily until stage “b” where the bonded interface starts to propagate abruptly and fails immediately. Due to unstable crack propagation in 3ENF test, only the part from stage “c” to stage “b” in the R-curves of the tested specimens is obtained based on EGM and is shown in Fig. 22. The critical SERR for crack initiation $G_{IIc,tip}$ is obtained at stage “c” and increases gradually during the fracture process to $G_{IIc,tip} + G_{II,soft}$ at stage “b”. The FPZ length $FPZ_{II,soft}$ related to softening is represented by distance between point at stage “c” and point at stage “b” on the R-curves, see Fig. 22. $FPZ_{IIc,tip}$ is neglected attributed to its limited length while $FPZ_{IIc,br}$ remains unknown

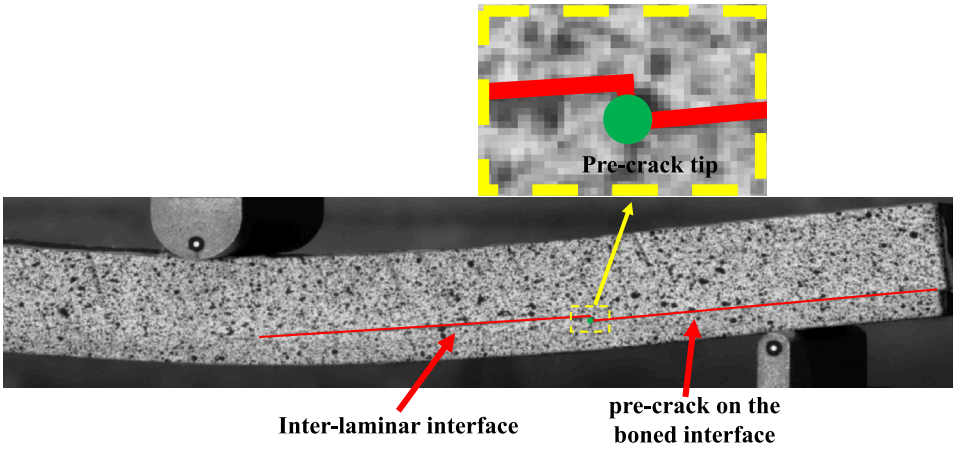

Fig. 15. Front view of specimen 3ENF-CU-S5 during test indicating the crack transition.

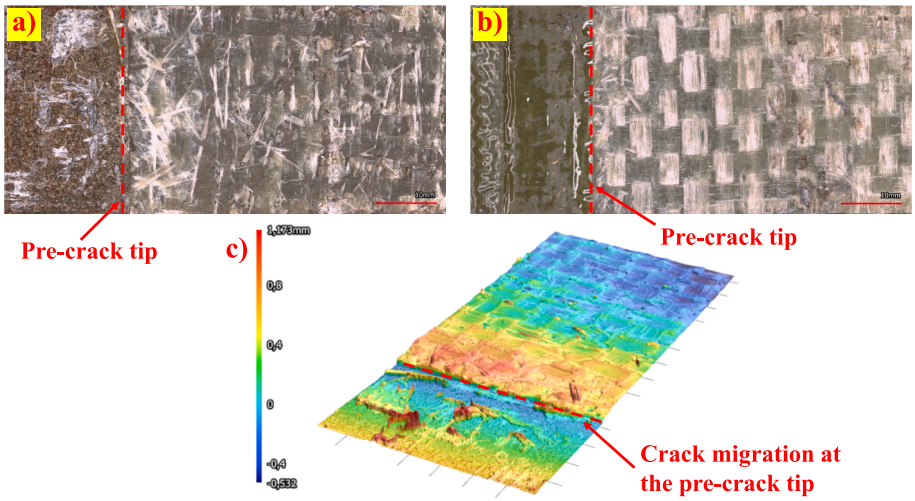

Fig. 16. Fracture surface morphology of specimen 3ENF-CU-S5: a) image of the fracture surface on the steel adherend; b) image of the fracture surface on the composite adherends; c) 3D scan of the fracture surface on the steel adherend.

Table 4
Overview of displacement/load values at the critical stages of the fracture process in 3ENF test vs 3ENF FEM.

Specimens or FE model	Onset of plasticity (stage "p")		Onset of cracking (stage "c")		Onset of bridging (stage "b")		Failure (stage "f")	
	Displacement (mm)	Load (N)	Displacement (mm)	Load (N)	Displacement (mm)	Load (N)	Displacement (mm)	Load (N)
3ENF-CL-S1	0.61	1335	1.59	3431	2.67	5394	–	–
3ENF-CL-S2	0.74	1597	1.72	3911	2.72	5918	–	–
3ENF-CL-S3	0.87	2042	1.64	3641	2.34	4932	–	–
Average (and COV [%])	0.74 (14.3)	1658 (17.6)	1.65 (3.2)	3661 (5.4)	2.58 (6.5)	5415 (7.4)	–	–
3ENF-FEM	0.75	1746	1.69	3789	2.54	5334	–	–
Deviation (%)	1.4	5.3	2.4	3.4	1.6	1.5	–	–

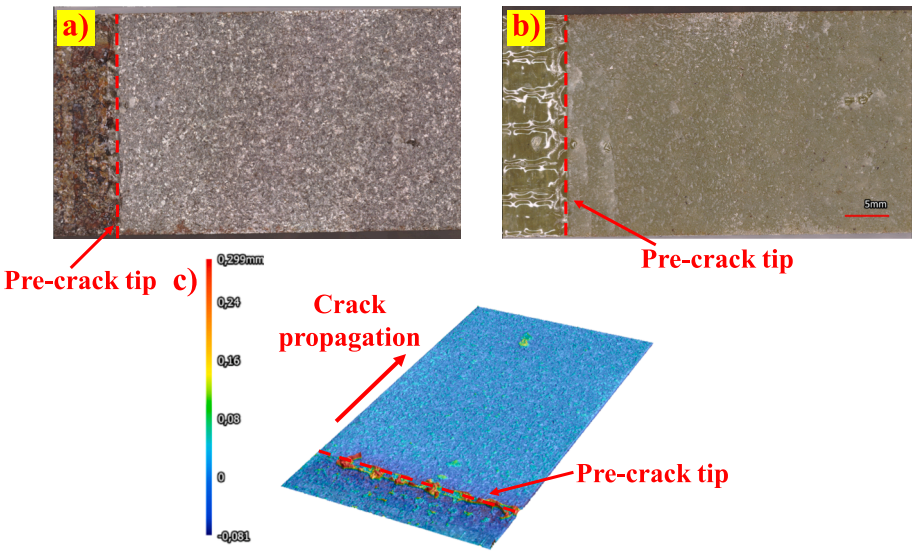

Fig. 17. Fracture surface morphology of specimen 3ENF-CL-S2: a) image of the fracture surface on the steel adherend; b) image of the fracture surface on the composite adherends; c) 3D scan of the fracture surface on the steel adherend.

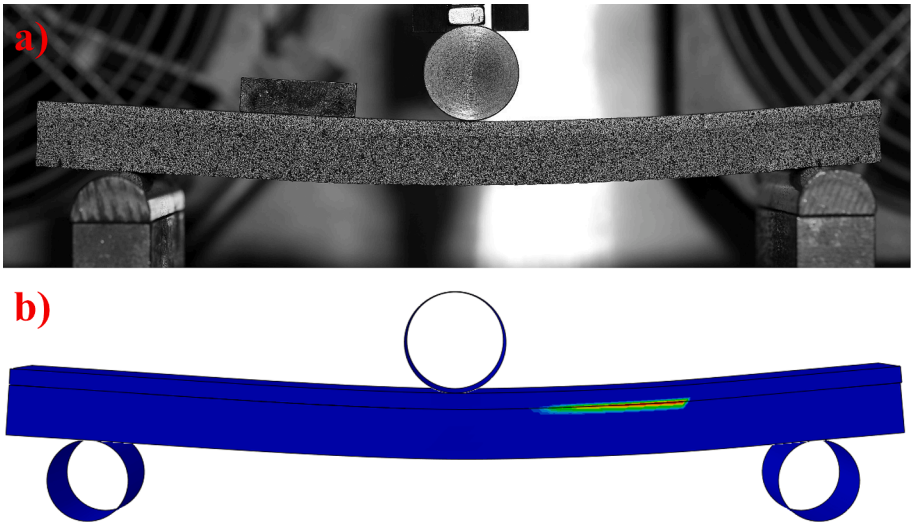

Fig. 18. Comparisons of failure modes in a) 3ENF tests and in b) 3ENF FEM at stage "g".

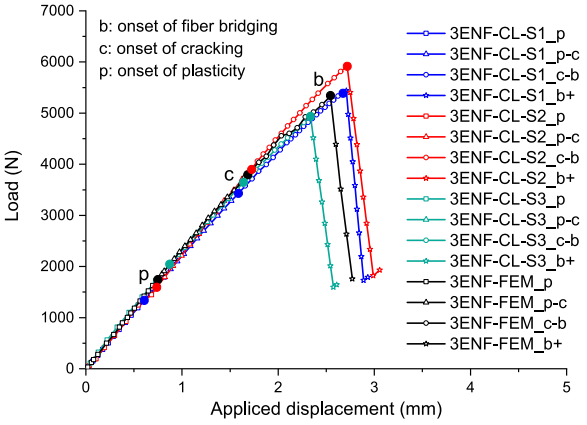

Fig. 19. Comparison of load–displacement response in 3ENF test vs modeling.

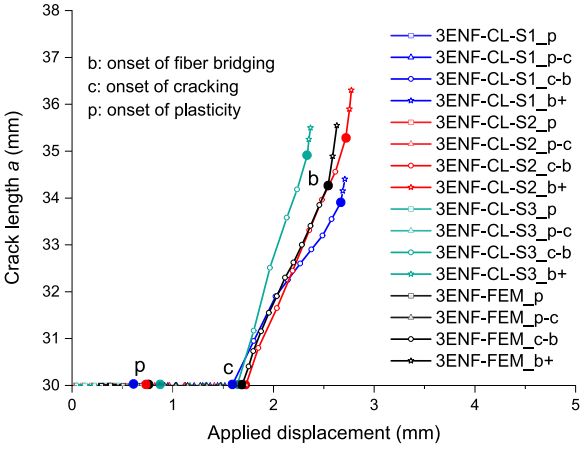

Fig. 20. Comparison of *a*-displacement relation in 3ENF test vs modeling.

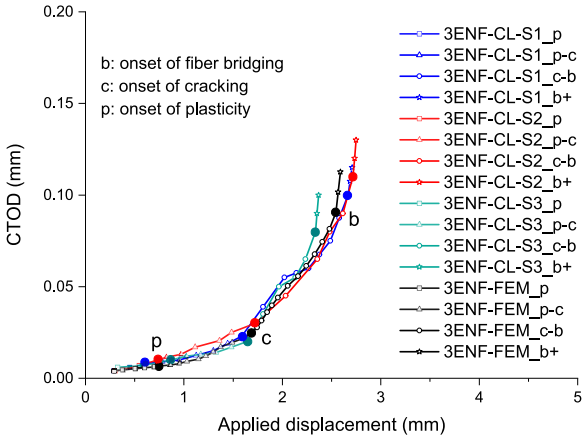

Fig. 21. Comparison of CTOD-displacement relation in 3ENF test vs modeling.

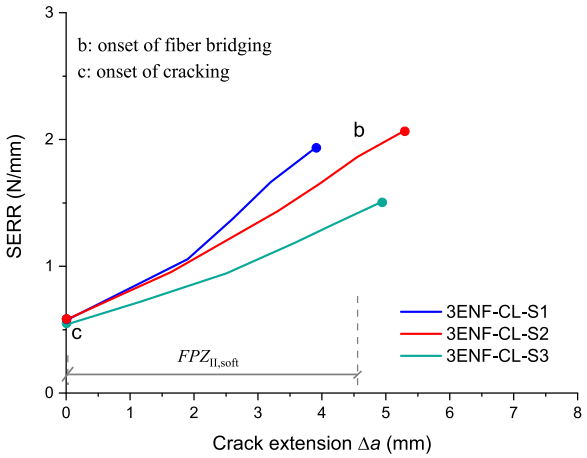

Fig. 22. R-curves of 3 specimens in 3ENF tests with composite laminate as lower adherend.

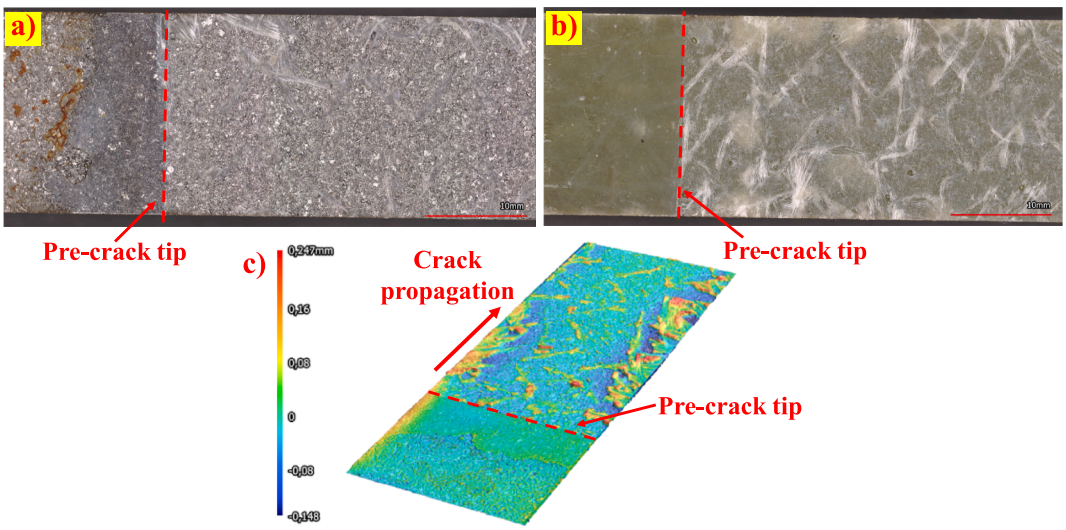

Fig. 23. Fracture surface morphology of specimen 4ENF-CL-S1: a) image of the fracture surface on the steel adherend; b) image of the fracture surface on the composite adherends; c) 3D scan of the fracture surface on the steel adherend.

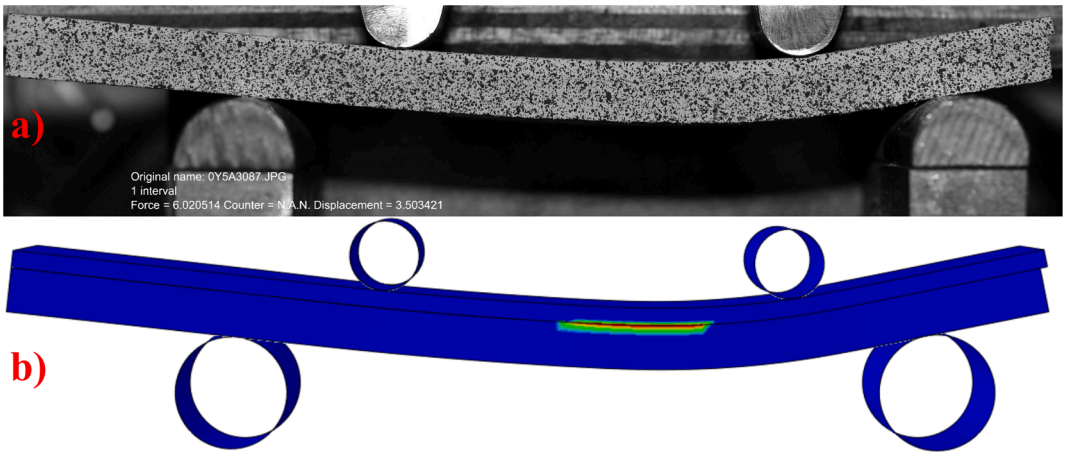

Fig. 24. Comparisons of failure modes in a) 4ENF tests and in b) 4ENF FEM at stage "f".

as a consequence of unstable crack propagation.

To investigate the influence of the pre-crack length to the half span ratio a_0/L on the instability of crack propagation in 3ENF tests, additional 3ENF tests were conducted on 2 specimens (3ENF-CL-S4/5). These specimens originate from the same production batch and possess identical geometry, test set-up and loading scenarios as the specimens (3ENF-CL-S1/2/3) in test series 2. They were tested using the pre-crack length to the half span ratio a_0/L of 0.7 recommended in the current literature [12,13] by decreasing the span length.

The values of $G_{IIc,tip}$, $G_{IIc,tip} + G_{II,soft}$, and $FPZ_{II,soft}$ in three 3ENF specimens (3ENF-CL-S1/2/3) with a_0/L of 0.33 are summarized in Table 5. It can also been seen in Table 5 that the average values of $FPZ_{II,soft}$ is approximately 5 mm. Moreover, the crack propagation in the test specimens 3ENF-CL-S4/5 with a_0/L=0.7 is still observed to be unstable, contrary to what was expected based on the literature. The possible reasons are: 1) the recommendation of pre-crack length to half span ratio is specific to the monolithic specimens but not applicable to bi-material interface cracking; 2) the large thickness to span ratio ($h/2L$) of test specimens might contribute to this instability; 3) there is a complete absence of fiber bridging in 3ENF specimens. The fracture properties of specimens 3ENF-CL-S4/5 are also summarized in Table 5.

6.3. Test results of 4ENF specimens

To prevent unstable crack growth observed in 3ENF tests, 4ENF tests were performed in test series 3. Local bending moments in arms of adherends around the crack tip are constant and independent of the crack length which leads to stable crack propagation in 4ENF configuration. The load–displacement response of the 4ENF specimens is shown in Fig. 25 where the critical stages are identified, and the associated values of applied displacement and load are summarized in Table 6. The fracture morphology is shown in Fig. 23. It exhibits more pronounced fiber bridging than in 3ENF tests (see Fig. 17), a consequence of nesting of the chopped strand mat in the first laminate ply with the micro profile of steel surface roughness. The more pronounced fiber bridging behavior in 4ENF specimens is due to the increase steel roughness in the production batch compared to that of 3ENF specimens. It can be seen in Fig. 25 that onset of plasticity (stage "p") corresponds to the elastic load limit at approximately 1700 N followed by crack initiation at approximately 3000 N (stage "c"). Different from 3ENF tests, the applied load increases consistently in 4ENF tests from stage "c" to stage "f" within the load range of 6000–7000 N as the pre-crack tip propagates consistently. This difference can be explained in two aspects: 1) the bending moment at the present crack tip is independent of the crack length a in 4ENF loading (see Equation (13) and Equation (14) which is favorable for stable crack propagation; 2) fiber bridging behavior in 4ENF tests (see Fig. 23) is more pronounced compared to 3ENF

Table 5
Overview values of fracture resistance and FPZ length in 3ENF test.

Specimens with a_0/L=0.33	SERR (N/mm)		$FPZ_{II,soft}$ (mm)
	$G_{IIc,tip}$	$G_{IIc,tip} + G_{II,soft}$	
3ENF-CL-S1	0.57	1.93	3.9
3ENF-CL-S2	0.58	2.07	5.3
3ENF-CL-S3	0.54	1.50	4.9
Average (and COV [%])	0.56 (3.0)	1.83 (13.2)	4.7 (12.5)
Specimens with a_0/L=0.7	SERR (N/mm)		$FPZ_{II,soft}$ (mm)
	$G_{IIc,tip}$	$G_{IIc,tip} + G_{II,soft}$	
3ENF-CL-S4	0.53	1.57	3.9
3EFN-CL-S5	0.55	1.34	4.2

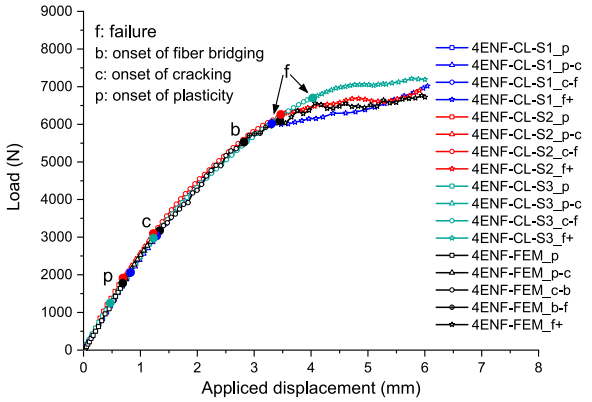

Fig. 25. Comparison of load–displacement response in 4ENF test vs modeling.

Table 6
Overview of displacement/load values at the critical stages of the fracture process in 4ENF test vs 4ENF FEM.

Specimens or FE model	Onset of plasticity (stage "p")		Onset of cracking (stage "c")		Onset of bridging (stage "b")		Failure (stage "f")	
	Displacement (mm)	Load (N)	Displacement (mm)	Load (N)	Displacement (mm)	Load (N)	Displacement (mm)	Load (N)
4ENF-CL-S1	0.83	2063	1.29	3032	–	–	3.31	6021
4ENF-CL-S2	0.70	1908	1.23	3088	–	–	3.46	6261
4ENF-CL-S3	0.47	1243	1.24	2975	–	–	4.44	6958
Average (and COV [%])	0.67 (22.3)	1738 (20.5)	1.25 (2.1)	3032 (1.5)	–	–	3.74 (13.4)	6413 (6.2)
4ENF-FEM	0.70	1768	1.34	3175	2.82	5528	3.45	6085
Deviation (%)	4.5	1.7	7.2	4.7	–	–	7.8	5.1

tests (see Fig. 17) as a consequence of increase steel roughness. Therefore, 4ENF specimens have a greater ability to engage in stable propagation than 3ENF specimens.

Fig. 26 and Fig. 27 illustrate the development of the crack length a and the CTOD at the pre-crack tip with the increased applied displacement during the tests, respectively. Similar to 3ENF tests, the pre-crack tip starts to open at stage "p", but the opening displacement is limited (less than 0.02 mm). After the crack is initiated at stage "c", the crack length a and the CTOD develop gradually until stage "f" where these two variables increase at a constant rate. This indicates that FPZ for crack propagation is fully developed, and crack starts to propagate in a stable manner. Based on the EGM, the mode II SERR of the composite-steel bonded interface was calculated and its relation with the crack extension Δa, i.e. the R-curve, is shown in Fig. 28. It can be seen that the critical SERR for crack initiation $G_{\mathrm{IIc,tip}}$ is approximately 0.9 N/mm on average obtained at stage "c", and increases gradually during the fracture process to $G_{\mathrm{IIc}} = 5.4$ N/mm on average at stage "f", defined as the critical SERR for crack propagation. The summation of the FPZ length due to softening $FPZ_{\mathrm{II,soft}}$ and due to fiber bridging $FPZ_{\mathrm{II,br}}$ refers to the distance between point at stage "c" and point at stage "f" on the R-curves, while $FPZ_{\mathrm{IIc,tip}}$ is neglected. The values of $G_{\mathrm{IIc,tip}}$, G_{IIc} and $FPZ_{\mathrm{II,soft}} + FPZ_{\mathrm{II,br}}$ in three 4ENF specimens are summarized in

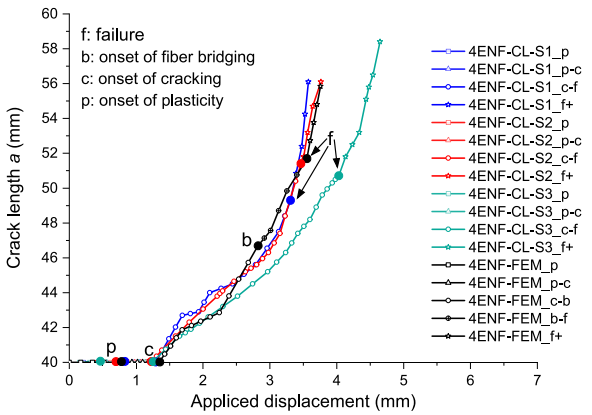

Fig. 26. Comparison of a-displacement relation in 4ENF test vs modeling.

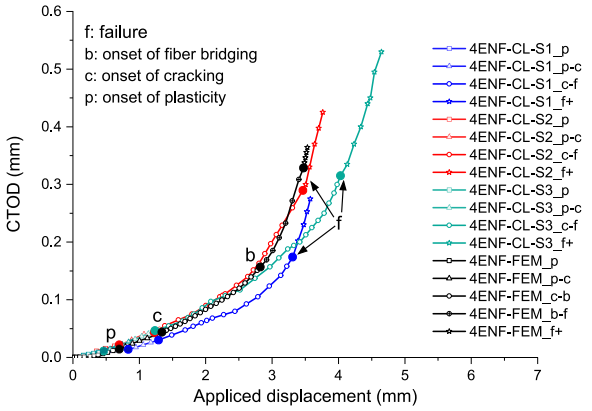

Fig. 27. Comparison of CTOD-displacement relation in 4ENF test vs modeling.

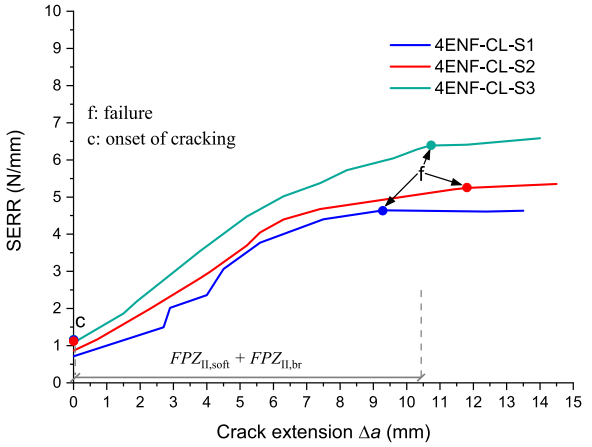

Fig. 28. R-curves of 3 specimens in 4ENF tests.

Table 7. The average values of $FPZ_{II,soft} + FPZ_{II,br}$ in mode II fracture is approximately 10 mm.

6.4. Validation of 3ENF and 4ENF FEM

It can be seen in Fig. 19 and Fig. 25 that the load–displacement behavior from the numerical model (black curves) match well with the testing curves in terms of elasticity and non-linear behavior in both 3ENF and 4ENF results. Comparison of load and applied displacement values at critical stages are presented in Table 4 and Table 6 where the deviation of numerical results from average testing results are within 8 %. Therefore, it can be concluded that good match is reached in terms of global response in 3ENF modeling vs 3ENF tests, and in 4ENF modeling vs 4ENF tests. The numerical load–displacement curve in Fig. 25 illustrates that stage "f" is reached from stage "b" through only 500 N load increase. This indicates that the contribution of fiber bridging to fracture resistance is quite limited and the majority of the resistance after crack initiation comes from the softening phenomenon from stage "c" to stage "b" in mode II failure. Fig. 18 compares the failure modes regarding crack propagation states and specimen deflection between the 3ENF test and its corresponding 3ENF modeling. Similarly, Fig. 24 illustrates such comparison between the 4ENF test and its respective 4ENF modeling. In both cases, it can be concluded that good agreement is reached in terms of failure modes.

Table 7
Overview values of fracture resistance and FPZ length in 4ENF test.

Specimens	SERR (N/mm)		$FPZ_{II,soft} + FPZ_{II,br}$ (mm)
	$G_{IIc,tip}$	G_{IIc}	
4ENF-CL-S1	0.72	4.64	9.3
4ENF-CL-S2	0.86	5.20	11.4
4ENF-CL-S3	1.08	6.39	10.7
Average (and COV[%])	0.89 (16.7)	5.41 (13.5)	10.5 (8.3)

In Fig. 20–Fig. 21 and in Fig. 26–Fig. 27, the crack length a and the CTOD vs applied displacement obtained from the FE models are plotted and compared with the curves from 3ENF and 4ENF tests, respectively. In both cases good matches of the crack length and the CTOD in tests and in FEM are achieved. It can also be seen in Fig. 26 that the crack extension Δa obtained from 4ENF FEM is approximately 11.5 mm which matches well to the average value from 4ENF tests. Therefore, it can be concluded that good agreement of the failure process is achieved in 3ENF modeling vs 3ENF tests, and in 4ENF modeling vs 4ENF tests. Fig. 13 illustrates that the longitudinal position of the present crack tip varies across the width of the specimen with a concave shape. This is due to the anticlastic bending of the specimen affected by both material properties (Poisson's ratio) and geometry of the specimens [45,46,62–64]. In the ENF experiments, the crack location can only be captured by the camera at the edge of the specimen. From the FE model, the difference in crack length between the middle and the edge locations was measured, and the value was found to be 0.4 mm.

It should be noted that the load roller radius is greater than the support roller radius in 3ENF tests, while in 4ENF tests, the support roller radius is larger than the load radius. The discrepancy in the radius is due to the availability of the test setup in the laboratory. However, the impact of the roller radius on the modelling results has been carefully investigated. In finite element modelling, the exact and actual radius of the support and load rollers were used as in the experiments. A parametric study was conducted by changing the roller radius and it was found that the radius significantly affects the development of fracture parameters. Therefore, it is crucial to use the actual radius of the support and load rollers in the FE models, as in the experiments.

6.5. *Effects of mode mixity and friction*

As mentioned in the Introduction section, mode mixity inherently exists in the bi-material interface cracking. Generally, two design criteria are proposed to achieve pure mode failure: equal axial strains along the interface or equal bending rigidities. Moreover, the effects of friction on the calculation of the mode II fracture toughness cannot be ignored.

In this subsection, supplementary FEA was conducted using the Virtual Crack Closure Technique (VCCT) [65] on both 3ENF and 4ENF specimens to assess mode mixity and friction effects. To evaluate the mode mixity, VCCT analysis was first performed in modeling of 3ENF and 4ENF scenarios without friction. Afterwards, the coefficient of friction (COF) was introduced to quantify the friction effects on calculating fracture toughness. Fig. 29 illustrates that the input values of COF are 0.2 within the pre-crack inset (between composites and non-adhesive Teflon-based tape) and 0.55 in the bonded regions (between composites and steel roughness profile), respectively. These values were obtained from COF tests performed by the authors, which are not included in this paper.

In the 3ENF configuration, stages "c" and "g" were selected for VCCT analysis while stage "c" and "f" were chosen in modeling the 4ENF configuration. Table 8 provides the mode I and mode II contributions to the total critical SERR from VCCT, the associated mode mixity G_{II} / G, as well as the difference of G between EGM and VCCT. It is observed that the introduced mode mixity is rather small (no more than 1.2 %) in all configurations, implying that the specimen design in the current study is accurate enough for nearly pure mode II conditions. Moreover, the difference in the critical SERR calculated by EGM and VCCT is relatively small (less than 7 %). It is worth noting that there are limitations [66] in accurately determining the mode mixity based on VCCT which is a liner elastic fracture mechanics-based method. The non-linearity related to formation of the FPZ cannot be captured by this method. Alternative approaches, such as the thick level set interface method [67] may be more suitable for capturing this aspect. But the current research primarily focuses on the difference of influence of friction in 3ENF and 4ENF tests. To address this, VCCT is utilized along with an Explicit solver capable of handling complex contact interactions and frictions in both the insert and crack regions. By measuring the COF in these regions, the authors can utilize this combined LEFM method and contact mechanics to analyze the partial non-linearity in the 4ENF modelling. It is worth noting that in the EGM method, steel yielding cannot be explicitly taken into account, and the behavior of steel is assumed to be linear. However, in finite element modeling using VCCT analysis, the non-linear properties of steel are taken into account. We conducted VCCT analysis with multiple crack lengths. If there were a crack length at which the bending moment in the steel arm exceeded the yielding capacity of the steel plate, this would already occur and reduce the strain energy release rate (SERR) acting on the interface. The SERR determined by VCCT without friction can be compared to the value obtained from EGM, as shown in Table 8. The difference indicates the potential effect of steel yielding.

Table 9 compares the critical SERR values calculated by VCCT with and without the introduction of friction. It can be concluded that friction effects on calculating fracture toughness in 3ENF tests are negligible (less than 4 %), while the influence is significantly larger in 4ENF tests (8 %~13 %).

7. Conclusions

In the present research study, 3ENF and 4ENF experiments with help of FEM were used to explain and quantify mode II fracture

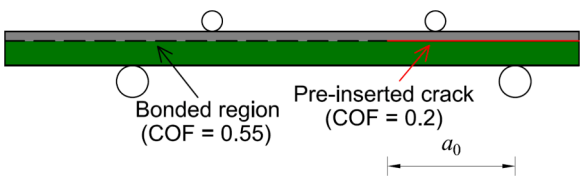

Fig. 29. Set-up of coefficient of friction in VCCT modeling – 4ENF as an example.

Table 8
Overview of mode I, mode II, and total critical SERR values in 3ENF and 4ENF scenarios.

Specimen configuration	Critical stages	EGM	VCCT_w/o friction				Difference, VCCT-EGM (%)
		G (N/mm)	G_I (N/mm)	G_{II} (N/mm)	G (N/mm)	G_{II} / G (%)	
3ENF	Stage "c"	0.561	0.007	0.568	0.575	98.8	2.4
	Stage "g"	1.833	0.013	1.788	1.801	99.3	1.8
4ENF	Stage "c"	0.886	0.004	0.918	0.922	99.5	4.0
	Stage "f"	5.412	0.015	5.769	5.784	99.7	6.4

Table 9
Effects of friction on the critical SERR values in 3ENF and 4ENF configurations.

Specimen configuration	Critical stages	VCCT_w/o friction	VCCT_w/ friction	Difference (%)
		G_{II} (N/mm)	G_{II} (N/mm)	
3ENF	Stage "c"	0.568	0.549	3.4
	Stage "g"	1.788	1.757	1.8
4ENF	Stage "c"	0.918	0.800	12.9
	Stage "f"	5.769	5.254	8.9

behavior of bi-material glass fiber composite-steel bonded interface. The crack length a and the crack tip opening displacement (CTOD) during the tests were obtained by novel approaches to analysis of digital image correlation (DIC) measurement data while the strain energy release rate (SERR) was calculated through the extended global method (EGM). A four-linear cohesive law featuring onset of plasticity, cracking and bridging, and final failure was proposed and used in the 3ENF and 4ENF FE models to accurately simulate the mode II fracture behavior. These findings offer valuable insights into the ductile fracture behavior and characterization of bi-material bonded joints, enriching our understanding of their physical failure in mode II. Moreover, they streamline the process of assessing bi-material bonded joints. Based on the experimental results and the numerical work, the following conclusions are drawn:

1) To ensure crack propagation on the composite-steel bonded interface instead of transition into the inter-laminar interface due to tensile bending stresses, composite laminate should be designed as the lower adherend (with respect to the load direction) in 3ENF and 4ENF experiments. 3ENF test provides good insight into softening behavior while 4ENF shows to be more useful to quantify fiber bridging. It is important to choose the proper types of bi-material interface tests that are suitable for the types of loading and geometry being designed for bonded joints.
2) The average critical SERR for crack initiation $G_{\mathrm{IIc,tip}}$ in 3ENF and 4ENF specimens is 0.56 N/mm and 0.89 N/mm, respectively. The major reason for the difference is not the testing methodology but the steel roughness. 4ENF specimens were produced with increased steel roughness and therefore have improved fracture toughness than 3ENF specimens. The mode II fracture toughness at the crack initiation affects the ultimate resistance of single-lap or double-lap joints, but it has no influence on the ultimate resistance of damage tolerant bonded joints, governed by crack propagation, such as wrapped composite joints.
3) The average critical SERR for crack propagation G_{IIc} in 3ENF and 4ENF specimens is 1.9 N/mm and 5.4 N/mm, respectively. Similarly, the major reason for this difference is the steel roughness and bonding properties in those two batches of specimens. 4ENF specimens were produced with increased steel roughness and therefore have improved fracture toughness than 3ENF specimens. 4ENF tests provide a better opportunity to capture the very high fracture toughness of 5.4 N/mm with the 4ENF specimens with increase steel roughness in good bonding properties. The mode II fracture toughness at the crack propagation has a significant influence on the ultimate load resistance of wrapped composite joints.
4) A four-linear traction-separation law is proposed to describe the mode II interface behavior. It describes three distinct phenomena: 1) crack tip deformation, 2) softening (newly proposed) and 3) fiber bridging. The fracture morphology indicates that fiber bridging is not governing. The non-linear load–displacement behavior is attributed to the softening phenomenon as a consequence of pull-out of resin from valleys in the micro profile of steel surface roughness. The characteristic stages in the four-linear cohesive law are determined by the global and detailed results of 3ENF and 4ENF tests and modeling.
5) A new "shear strain scaling method" is proposed based on DIC measurements to quantify the crack length in the 3ENF and 4ENF tests. DIC sectioning method was introduced and proved to be effective to evaluate usually challenging mode II CTOD.
6) Friction effects on the calculation of SERR are more pronounced in 4ENF tests (up to 13 %) compared to 3ENF tests (up to 3.5 %). In all test configurations, nearly mode II conditions were achieved using the current specimen design, with a mode mixity ratio of no less than 98.8 %.

The presented characterization and understanding of the bi-material interface behavior goes beyond the first intended application in wrapped composite joints and are valuable for the wider field of engineering, such as aerospace, automotive and others.

CRediT authorship contribution statement

Pei He: Writing – original draft, Visualization, Investigation, Formal analysis, Data curation. **Mathieu Koetsier:** Writing – review & editing, Data curation. **Vasileios Mylonopoulos:** Data curation. **Marko Pavlovic:** Writing – review & editing, Supervision, Project administration, Methodology, Funding acquisition, Conceptualization.

Declaration of competing interest

The authors declare that they have no known competing financial interests or personal relationships that could have appeared to influence the work reported in this paper.

Data availability

Data will be made available on request.

Acknowledgement

This research is supported by NWO Demonstrator project grant 16949 and RVO project Topsector Energiesubsidie van het Ministerie van Economische Zaken through WrapNode-I project. The first author would also like to express his gratitude for the financial support from China Scholarship Council (CSC) under grant number of 201806260242. The authors are grateful for the acknowledge provision and fabrication of the wrapped composite joints by Tree Composites b.v., Versteden b.v.and Ask Romein b.v. The authors are very grateful for the assistance of technicians from Steven Lab II of TU Delft.

References

[1] M. Pavlovic, M. Veljkovic, and P. Bogers, "Method for making a virgin joint between two separate structural hollow sections, and such a virgin joint," 11,542,708, 2019 [Online]. Available: https://patents.google.com/patent/US11542708B2/en.
[2] P. He and M. Pavlovic, "Failure modes of bonded wrapped composite joints for steel circular hollow sections in ultimate load experiments," *Eng. Struct.*, vol. 254, no. August 2021, p. 113799, 2022, doi: 10.1016/j.engstruct.2021.113799.
[3] Feng W, Pavlovic M. Fatigue behaviour of non-welded wrapped composite joints for steel hollow sections in axial load experiments. Eng Struct 2021;vol. 249, no. October:113369. https://doi.org/10.1016/j.engstruct.2021.113369.
[4] He P, Arouche M, Koetsier M, Pavlovic M. Mode I fracture behavior of glass fiber composite-steel bonded interface – experiments and CZM. Compos Struct 2023; 330. https://doi.org/10.1016/j.compstruct.2023.117814.
[5] Russel A. Factors affecting the interlaminar fracture energy of graphite/epoxy laminates. Proc. 4th Int. Conf. Comp. Mater; 1982. Accessed: Mar. 08, 2023. [Online]. Available:.
[6] Russel A. On the measurement of mode II interlaminar fracture energies. Def Res Establ pacific, victoria BC 1982.
[7] ASTM International. "ASTM D7905/D7905M-14: standard Test Method for Determination of the Mode II Interlaminar Fracture Toughness of Unidirectional Fiber-Reinforced Polymer", *West Conshohocken*. PA ASTM Int 2014. https://doi.org/10.1520/D7905.
[8] Todo M, Jar PYB, Takahashi K. Initiation of a mode-II interlaminar crack from an insert film in the end-notched flexure composite specimen. Compos Sci Technol 2000;60(2):263–72. https://doi.org/10.1016/S0266-3538(99)00119-0.
[9] de Moura MFSF, Campilho RDSG, Gonçalves JPM. Pure mode II fracture characterization of composite bonded joints. Int J Solids Struct 2009;46(6):1589–95. https://doi.org/10.1016/j.ijsolstr.2008.12.001.
[10] Chen CC, Linzell DG. Modeling end notched flexure tests to establish cohesive element Mode II fracture parameters. Eng Fract Mech 2010;77(8):1338–47. https://doi.org/10.1016/j.engfracmech.2010.03.017.
[11] Arrese A, Carbajal N, Vargas G, Mujika F. A new method for determining mode II R-curve by the End-Notched Flexure test. Eng Fract Mech 2010;77(1):51–70. https://doi.org/10.1016/j.engfracmech.2009.09.008.
[12] Carlsson LA, Gillespie JW, Pipes RB. On the Analysis and Design of the End Notched Flexure (ENF) Specimen for Mode II Testing. J Compos Mater 1986;20(6): 594–604. https://doi.org/10.1177/002199838602000606.
[13] Davies P, Casari P, Carlsson LA. Influence of fibre volume fraction on mode II interlaminar fracture toughness of glass/epoxy using the 4ENF specimen. Compos Sci Technol 2005;65(2):295–300. https://doi.org/10.1016/j.compscitech.2004.07.014.
[14] Blackman BRK, Kinloch AJ, Paraschi M. The determination of the mode II adhesive fracture resistance, GIIC, of structural adhesive joints: an effective crack length approach. Eng Fract Mech 2005;vol. 72, no. 6 SPEC. ISS:877–97. https://doi.org/10.1016/j.engfracmech.2004.08.007.
[15] Brunner AJ, Blackman BRK, Davies P. A status report on delamination resistance testing of polymer-matrix composites. Eng Fract Mech 2008;75(9):2779–94. https://doi.org/10.1016/j.engfracmech.2007.03.012.
[16] Martin RH, Davidson BD. Mode II fracture toughness evaluation using four point bend, end notched flexure test. Plast Rubber Compos Process Appl 1999;28(8): 401–6. https://doi.org/10.1179/146580199101540565.
[17] Schuecker C, Davidson BD. Evaluation of the accuracy of the four-point bend end-notched flexure test for mode II delamination toughness determination. Compos Sci Technol 2000;60(11):2137–46. https://doi.org/10.1016/S0266-3538(00)00113-5.
[18] Schuecker C, Davidson BD. Effect of friction on the perceived mode II delamination toughness from three-and four-point bend end-notched flexure tests. Composite Structures: Theory and Practice. ASTM International; 2001.
[19] Davidson P, Waas AM, Yerramalli CS. Experimental determination of validated, critical interfacial modes I and II energy release rates in a composite sandwich panel. Compos Struct 2012;94(2):477–83. https://doi.org/10.1016/j.compstruct.2011.08.007.
[20] Alía C, Arenas JM, Suárez JC, Narbón JJ, Ocaña R. ENF test in the adhesive bonding of aluminium-composite joints and evaluation of its reliability with Weibull distribution. J Adhes Sci Technol 2013;27(11):1236–46. https://doi.org/10.1080/01694243.2012.736853.
[21] Alía C, Arenas JM, Suárez JC, Ocaña R, Narbón JJ. Mode II fracture energy in the adhesive bonding of dissimilar substrates: carbon fibre composite to aluminium joints. J Adhes Sci Technol 2013;27(22):2480–94. https://doi.org/10.1080/01694243.2013.787516.
[22] Arenas JM, Ocaña R, Alía C, Narbón JJ, Islán M. Fracture energy in structural adhesive joints of composite-aluminum under adverse environments conditions. J Adhes Sci Technol 2014;28(2):201–14. https://doi.org/10.1080/01694243.2013.833404.
[23] Ouyang Z, Li G. Nonlinear interface shear fracture of end notched flexure specimens. Int J Solids Struct 2009;46(13):2659–68. https://doi.org/10.1016/j.ijsolstr.2009.02.011.
[24] Ning H, et al. Investigation on mode-II interface fracture toughness of CFRP/Al laminates toughened by VGCF interleaves. J Mater Sci 2015;50(4):1915–23. https://doi.org/10.1007/s10853-014-8755-5.

[25] W. Wang, S. T. De Freitas, J. A. Poulis, and D. Zarouchas, "A review of experimental and theoretical fracture characterization of bi-material bonded joints," *Compos. Part B Eng.*, vol. 206, no. October 2020, p. 108537, 2021, doi: 10.1016/j.compositesb.2020.108537.

[26] Ouyang Z, Ji G, Li G. On approximately realizing and characterizing pure mode-I interface fracture between bonded dissimilar materials. J Appl Mech Trans ASME 2011;78(3):pp. https://doi.org/10.1115/1.4003366.

[27] Z. Ouyang, G. Ji, G. Li, S. Ibekwe, and S. Pang, "A new idea of pure mode-I fracture test of bonded bi-materials," in *Proceedings of the ASME 2010 Pressure Vessels & Piping Division / K-PVP Conference*, 2010.

[28] Zambelis G, Da Silva Botelho T, Klinkova O, Tawfiq I, Lanouette C. Evaluation of the energy release rate in mode I of asymmetrical bonded composite/metal assembly. Eng Fract Mech 2018;190:175–85. https://doi.org/10.1016/j.engfracmech.2017.12.007.

[29] Boeman RG, Erdman DL, Klett LB, Lomax RD. A practical test method for mode I fracture toughness of adhesive joints with dissimilar substrates. SAMPE-ACCE-DOE Adv Compos Conf 1999:1–9.

[30] Jiang Z, Wan S, Wu Z. Calculation of energy release rate for adhesive composite/metal joints under mode-I loading considering effect of the non-uniformity. Compos Part B Eng 2016;95:374–85. https://doi.org/10.1016/j.compositesb.2016.04.001.

[31] M. Khoshravan and F. Asgari Mehrabadi, "Fracture analysis in adhesive composite material/aluminum joints under mode-I loading; Experimental and numerical approaches," *Int. J. Adhes. Adhes.*, vol. 39, pp. 8–14, 2012, doi: 10.1016/j.ijadhadh.2012.06.005.

[32] Shimamoto K, Sekiguchi Y, Sato C. Effects of surface treatment on the critical energy release rates of welded joints between glass fiber reinforced polypropylene and a metal. Int J Adhes Adhes 2016;67:31–7. https://doi.org/10.1016/j.ijadhadh.2015.12.022.

[33] Shimamoto K, Sekiguchi Y, Sato C. The critical energy release rate of welded joints between fiber-reinforced thermoplastics and metals when thermal residual stress is considered. J Adhes 2016;92(4):306–18. https://doi.org/10.1080/00218464.2015.1031339.

[34] F. Mujika, P. Tsokanas, A. Arrese, P. S. Valvo, and L. F. M. da Silva, "Mode decoupling in interlaminar fracture toughness tests on bimaterial specimens," *Eng. Fract. Mech.*, vol. 290, no. June, p. 109454, 2023, doi: 10.1016/j.engfracmech.2023.109454.

[35] Shahverdi M, Vassilopoulos AP, Keller T. Mixed-Mode I/II fracture behavior of asymmetric adhesively-bonded pultruded composite joints. Eng Fract Mech 2014;115:43–59. https://doi.org/10.1016/j.engfracmech.2013.11.014.

[36] Williams JG. On the calculation of energy release rates for cracked laminates. Int J Fract 1988;36(2):101–19. https://doi.org/10.1007/BF00017790.

[37] Arouche MM, Wang W, De Freitas ST. Strain-based methodology for mixed-mode I + II fracture : a new partitioning method for bi- material adhesively bonded joints. J Adhes 2019;95(5–7):385–404. https://doi.org/10.1080/00218464.2019.1565756.

[38] De Morais AB, Pereira AB. Mixed mode I + II interlaminar fracture of glass / epoxy multidirectional laminates – Part 1: analysis. Compos Sci Technol 2006;66:1889–95. https://doi.org/10.1016/j.compscitech.2006.04.006.

[39] Shahverdi M, Vassilopoulos AP, Keller T. Mixed-mode quasi-static failure criteria for adhesively-bonded pultruded GFRP joints. Compos Part A Appl Sci Manuf 2014;59:45–56. https://doi.org/10.1016/j.compositesa.2013.12.007.

[40] Shahverdi M, Vassilopoulos AP, Keller T. Mixed-Mode I/II fracture behavior of asymmetric composite joints. Procedia Struct Integr 2016;2:1886–93. https://doi.org/10.1016/j.prostr.2016.06.237.

[41] Cameselle-Molares A, Vassilopoulos AP, Renart J, Turon A, Keller T. Numerical simulation of two-dimensional in-plane crack propagation in FRP laminates. Compos Struct 2018;200(April):396–407. https://doi.org/10.1016/j.compstruct.2018.05.136.

[42] Heidari-Rarani M, Shokrieh MM, Camanho PP. Finite element modeling of mode i delamination growth in laminated DCB specimens with R-curve effects. Compos Part B Eng 2013;45(1):897–903. https://doi.org/10.1016/j.compositesb.2012.09.051.

[43] Shokrieh MM, Heidari-Rarani M, Ayatollahi MR. Delamination R-curve as a material property of unidirectional glass/epoxy composites. Mater Des 2012;34:211–8. https://doi.org/10.1016/j.matdes.2011.08.006.

[44] S. Sugiman, P. D. Setyawan, S. Salman, and H. Ahmad, "Experimental and numerical investigation of the residual strength of steel-composites bonded joints: Effect of media and aging condition," *Compos. Part B Eng.*, vol. 173, no. October 2018, p. 106977, 2019, doi: 10.1016/j.compositesb.2019.106977.

[45] R. K. Joki, F. Grytten, B. Hayman, and B. F. Sørensen, "A mixed mode cohesive model for FRP laminates incorporating large scale bridging behaviour," *Eng. Fract. Mech.*, vol. 239, no. September 2019, p. 107274, 2020, doi: 10.1016/j.engfracmech.2020.107274.

[46] Joki RK, Grytten F, Hayman B, Sørensen BF. Determination of a cohesive law for delamination modelling - Accounting for variation in crack opening and stress state across the test specimen width. Compos Sci Technol 2016;128:49–57. https://doi.org/10.1016/j.compscitech.2016.01.026.

[47] K. Leffler, K. S. Alfredsson, and U. Stigh, "Shear behaviour of adhesive layers," vol. 44, pp. 530–545, 2007, doi: 10.1016/j.ijsolstr.2006.04.036.

[48] Sarrado C, Turon A, Costa J, Renart J. An experimental analysis of the fracture behavior of composite bonded joints in terms of cohesive laws. Compos Part A Appl Sci Manuf 2016;90:234–42. https://doi.org/10.1016/j.compositesa.2016.07.004.

[49] Svensson D, Alfredsson KS, Biel A, Stigh U. Measurement of cohesive laws for interlaminar failure of CFRP. Compos Sci Technol 2014;100:53–62. https://doi.org/10.1016/j.compscitech.2014.05.031.

[50] Shokrieh MM, Salamat-talab M, Heidari-rarani M. Effect of initial crack length on the measured bridging law of unidirectional E-glass / epoxy double cantilever beam specimens. J Mater 2014;55:605–11. https://doi.org/10.1016/j.matdes.2013.09.064.

[51] Shokrieh MM, Salamat-talab M, Heidari-rarani M. Dependency of bridging traction of DCB composite specimen on interface fiber angle. Theor Appl Fract Mech 2017;90:22–32. https://doi.org/10.1016/j.tafmec.2017.02.009.

[52] Arrese A, Boyano A, De Gracia J, Mujika F. A novel procedure to determine the cohesive law in DCB tests. Compos Sci Technol 2017;152:76–84. https://doi.org/10.1016/j.compscitech.2017.09.012.

[53] A. Arrese, N. Insausti, F. Mujika, M. Perez-Galmés, and J. Renart, "A novel experimental procedure to determine the cohesive law in ENF tests," *Compos. Sci. Technol.*, vol. 170, no. October 2018, pp. 42–50, 2019, doi: 10.1016/j.compscitech.2018.11.031.

[54] J. R. Rice, "A Path Independent Integral and the Approximate Analysis of Strain Concentration by Notches and Cracks," 2014.

[55] International Standards Organization. ISO 6892–1 International Standard INTERNATIONAL STANDARD ISO 6892–1:2009(E) Metallic materials — Tensile testing — Part 1: method of test at room temperature 1. Met Mater 2009;2009:64.

[56] International Standards Organization, "ISO 527-1:2012 - Plastics - Determination of tensile properties - Part 1: General principles," 2012, [Online]. Available: www.iso.org.

[57] International Standards Organization, "ISO 527-2:1996 – Plastics — Determination of tensile properties – Part 2: Test conditions for moulding and extursion plastics," 2009, [Online]. Available: http://www.chemshow.cn/UploadFile/datum/1000/huayangyq2008w_2009420145250792688.pdf.

[58] International Standards Organization, "ISO 14126:1999 - Fibre-reinforced plastic composites - Determination of compressive properties in the in-plane direction," 1999.

[59] International Standards Organization, "ISO 14129: 1997 Fibre-reinforced plastic composites — Determination of the in-plane shear stress/shear strain response, including the in-plane shear modulus and strength, by the plus or minus 45 degree tension test method," 1997.

[60] D. S. S. Corp., "ABAQUS/Explicit User's Manual.".

[61] W. Wang, R. Lopes Fernandes, S. Teixeira De Freitas, D. Zarouchas, and R. Benedictus, "How pure mode I can be obtained in bi-material bonded DCB joints: A longitudinal strain-based criterion," *Compos. Part B Eng.*, vol. 153, no. July, pp. 137–148, 2018, doi: 10.1016/j.compositesb.2018.07.033.

[62] Kotousov A, Lazzarin P, Berto F, Harding S. Effect of the thickness on elastic deformation and quasi-brittle fracture of plate components. Eng Fract Mech 2010;77(11):1665–81. https://doi.org/10.1016/j.engfracmech.2010.04.008.

[63] Z. Jiang, S. Wan, T. Keller, Z. Fang, and A. P. Vassilopoulos, "Influence of curved delamination front on R-curve of DCB specimen," *Compos. Struct.*, vol. 227, no. June, p. 111311, 2019, doi: 10.1016/j.compstruct.2019.111311.

[64] Davidson BD. An Analytical Investigation of Delamination Front Curvature in Double Cantilever Beam Specimens. J Compos Mater 1990;24(11):1124–37. https://doi.org/10.1177/002199839002401101.

[65] R. Krueger, "Virtual crack closure technique : History , approach , and applications," vol. 57, no. 2, pp. 109–143, 2013, doi: 10.1115/1.1595677.
[66] Conroy M, Kinloch AJ, Williams JG, Ivankovic A. Mixed mode partitioning of beam-like geometries : a damage dependent solution. Eng Fract Mech 2015;149: 351–67. https://doi.org/10.1016/j.engfracmech.2015.06.061.
[67] Latifi M, Van Der Meer FP, Sluys LJ. Composites : part A Fatigue modeling in composites with the thick level set interface method. Compos Part A 2017;101: 72–80. https://doi.org/10.1016/j.compositesa.2017.05.035.